

New advances in three-dimensional controlled-source electromagnetic inversion

Michael Commer and Gregory A. Newman

Lawrence Berkeley National Laboratory, Earth Sciences Division, 1 Cyclotron Rd., MS 90-116, Berkeley, CA 94720, USA.

E-mail: MCommer@lbl.gov, GANewman@lbl.gov

Accepted 2007 October 16. Received 2007 October 15; in original form 2007 May 20

SUMMARY

New techniques for improving both the computational and imaging performance of the three-dimensional (3-D) electromagnetic inverse problem are presented. A non-linear conjugate gradient algorithm is the framework of the inversion scheme. Full wave equation modelling for controlled sources is utilized for data simulation along with an efficient gradient computation approach for the model update. Improving the modelling efficiency of the 3-D finite difference (FD) method involves the separation of the potentially large modelling mesh, defining the set of model parameters, from the computational FD meshes used for field simulation. Grid spacings and thus overall grid sizes can be reduced and optimized according to source frequencies and source–receiver offsets of a given input data set. Further computational efficiency is obtained by combining different levels of parallelization. While the parallel scheme allows for an arbitrarily large number of parallel tasks, the relative amount of message passing is kept constant. Image enhancement is achieved by model parameter transformation functions, which enforce bounded conductivity parameters and thus prevent parameter overshoots. Further, a remedy for treating distorted data within the inversion process is presented. Data distortions simulated here include positioning errors and a highly conductive overburden, hiding the desired target signal. The methods are demonstrated using both synthetic and field data.

Key words: Numerical solutions; Inverse theory; Marine electromagnetics.

1 INTRODUCTION

Controlled source electromagnetic (CSEM) techniques use the electromagnetic energy of an artificial transmitter for detecting contrasts in the subsurface electrical conductivity. The bulk conductivity of rocks is dominated by the content of pore fluids, owing to the typically strong contrast between the highly resistive minerals and non-mineral substances, such as water, brine, or hydrocarbons. Even pore fluid substances can exhibit conductivity contrasts which are easily detectable by CSEM methods. While saline formation water has a typical resistivity range between 0.5 and 2 Ω m, the resistivity of hydrocarbon filled rocks can be up to two orders of magnitude larger (Schlumberger 1987). This has recently made the marine CSEM technique emerge with considerable potential of providing valuable complementary data to seismic hydrocarbon mapping. Seismic methods have a long and established history in hydrocarbon exploration, because they are proven to be very effective in mapping geological horizons with contrasting acoustic properties. CSEM methods, on the other hand, may delineate the different types of fluids within the horizon. With the marine CSEM method, a deep-towed electric bipole transmitter is used to excite a low-frequency (typically 0.1–10 Hz) electromagnetic signal that is measured on the sea floor over electric and magnetic field detectors, where larger transmitter–detector offsets can exceed 15 km (MacGregor & Sinha 2000; Eidesmo *et al.* 2002; Ellingsrud *et al.* 2002). With the current

technology, typical depths of investigation range from 1 to 4 km for offshore prospects.

Large-scale CSEM three-dimensional (3-D) geophysical imaging is now receiving considerable attention (Carazzone *et al.* 2005). While one-dimensional (1-D) modelling is relatively easy and trial and error 3-D forward modelling straight forward (Hoversten *et al.* 2006; Weiss & Constable 2006), the need for 3-D imaging is necessary as the search for hydrocarbons now increasingly occurs in highly complex and subtle offshore geological environments. This also further emphasizes the importance of combining the information obtained by CSEM surveys with existing 3-D seismic depth migration technologies (Hoversten *et al.* 2000). Faster 2-D CSEM imaging has some relevance to this problem. However, because of its assumption of 2-D geology, it cannot always be relied upon for a consistent treatment of the real environment, especially when measurements are made on survey grids specifically designed for 3-D imaging experiments (Carazzone *et al.* 2005).

In this study, we present techniques which further advance the 3-D CSEM inversion technique. Its inherently high computational requirements are a main obstacle to industrial applications. Whether finite volume, finite element, or finite difference (FD) techniques are used for simulating measurements in three dimensions, the modelling grids designed for approximating complex geology on a large scale usually become too computationally expensive for carrying out fast forward simulations. On the other hand, industrial large-scale

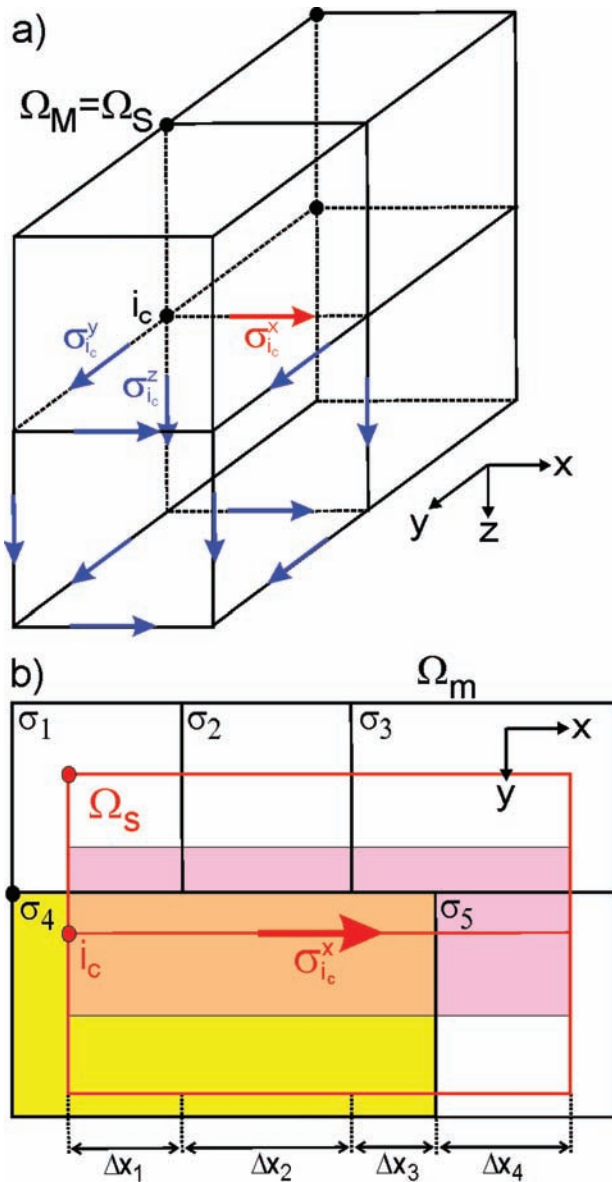


Figure 1. Illustration of scheme for mapping between model and simulation grid. (a) shows the equal-grid case. (b) illustrates the case of different grids in two dimensions.

3-D surveys with vast data volumes require both large modelling grids as well as many forward simulations; each CSEM transmitter location requires a separate forward calculation for simulating its response. To mitigate this problem, we present a method where the computational simulation grids are decoupled from an underlying common modelling grid. The latter represents the conductivity variation within the survey area. A simulation grid can then be adapted and thus optimized specifically to the geometries and offsets of a given transmitter and its detectors.

Since CSEM inversion is an ill-posed problem, implementation of constraints is important in reducing the solution ambiguity. We present new types of constraints, realized by model parameter transformation functions, to address this issue. Thereby, the electrical conductivity updates during the inversion process are restricted such that non-realistic results are suppressed.

A further technique outlined in this paper aims at efficiently using computing resources for the case of very large data sets. It is realized

by the combination of two different levels of parallelization. On the first level, the solution of the forward simulation problem is distributed among a bank of processors. This solution parallelization scales linearly up to a point where the necessary message passing required for completing matrix–vector multiplications in the iterative solution becomes dominant. To maintain the ability to use an arbitrarily large number of processors without a prohibitive message passing overhead, the solution of multiple forward problems is further distributed among groups of processor banks.

Furthermore, we have experimented with the source signature estimation applied to the CSEM inversion problem. While the source signature estimation problem is common in seismic waveform inversion, it also promises to alleviate data distortions in both amplitude and phase which might otherwise have negative effects on CSEM inverse modelling.

After introducing the theory for both the CSEM inverse and forward problems, the grid separation technique is outlined. Key to this approach is a proper material averaging scheme to map the conductivity parameters of the geological model to the computational grids used for the field solution in the forward problem. Consequently, the inverse problem requires an inverse mapping scheme to update the model parameters from the field solutions obtained on the computational simulation grids. In an earlier work (Commer & Newman 2005), we applied similar multigrid concepts to a finite-difference time-domain modelling scheme. This involved the averaging of material properties on a sequence of coarser simulation grids.

We next present various marine CSEM imaging scenarios using synthetic data to demonstrate the highly improved efficiency achieved by optimizing the simulation grids. This also includes inversion examples where the source signature estimation problem is solved within the inversion framework in order to correct for highly distorted data. At last, the inversion of real field data is presented, where the grid separation method is also further demonstrated. We use a data set of the Troll West Gas Province, located offshore Norway (Gray 1987). These measurements have been used for calibration purposes and modelling studies, since the data is known to contain strong signals caused by a large hydrocarbon reservoir (Johansen *et al.* 2005; Hoversten *et al.* 2006).

2 PROBLEM FORMULATION

We give a brief introduction of both the inverse and forward simulation problem. This shall provide the necessary framework for the concept of separating the model parameter grid from the computational simulation grids, presented later. A more detailed formulation of the EM inverse problem can be found in the works of Newman & Alumbaugh (1997, 2000) and Newman & Hoversten (2000).

The inverse problem is formulated by the minimization of the error functional,

$$\Phi = \frac{1}{2} [\mathbf{D}(\mathbf{d}^o - \mathbf{d}^p)]^H [\mathbf{D}(\mathbf{d}^o - \mathbf{d}^p)] + \frac{1}{2} \lambda (\mathbf{W}\mathbf{m})^H (\mathbf{W}\mathbf{m}), \quad (1)$$

where H denotes the transpose-conjugation operator. In the above expression, the predicted and observed data vectors are denoted by \mathbf{d}^p and \mathbf{d}^o , respectively, where each has N_d complex values. These vectors consist of electric or magnetic field values specified at the measurement points. The predicted data are determined through solution of the forward modelling problem, discussed below. We have also introduced a diagonal weighting matrix, $\mathbf{D}_{N_d \times N_d}$, into the error functional to compensate for noisy measurements; it is typically based on the inverse of the standard deviations of the measurements.

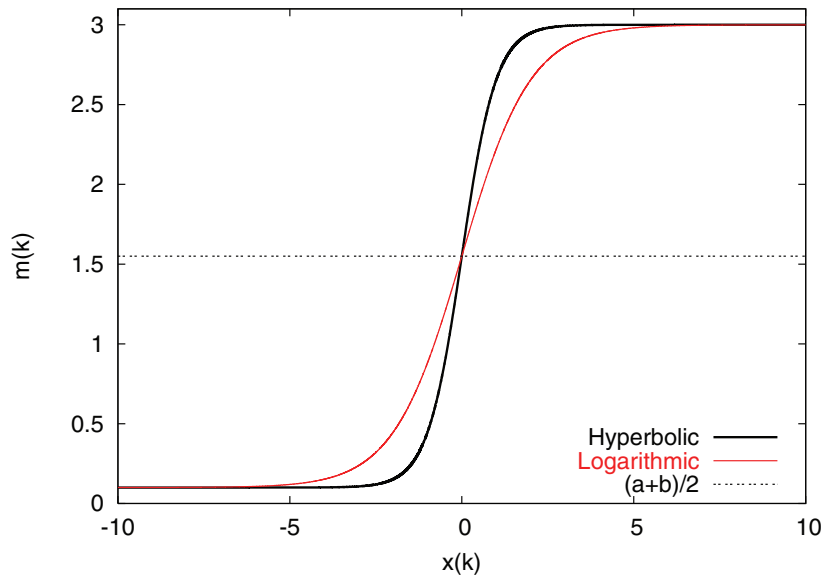


Figure 2. Graph of the hyperbolic and logarithmic inversion parameter transformations, given by eqs (11) and (14). The example shows the values of m_k for values of $a = 0.1$, $b = 3$ and $-10 < x_k < 10$.

Table 1. List of model and simulation grids for synthetic data generation and inversion.

Grid	Number of cells	Spacing Δ (m)	f (Hz)
Ω_M^0	$200 \times 200 \times 200$	50	
Ω_M	$134 \times 134 \times 134$	75	
Ω_S^1	$50 \times 50 \times 50$	200	0.25
Ω_S^2	$80 \times 80 \times 80$	125	0.75
Ω_S^3	$100 \times 100 \times 100$	100	1.25

In eq. (1), the properties of the model space are given by the vector \mathbf{m} . In our FD formulation, the model space consists of a 3-D mesh of rectangular cells, where the inversion domain can be represented by the whole model space or a subset of it. Each cell has electrical conductivities, dielectric and magnetic permeability properties assigned to it. Here, we only consider varying electrical conductivities σ as unknowns in the inverse problem.

The second term in eq. (1) is a regularization term which acts on the parameter unknowns and is required to stabilize the minimization of the error functional. Many choices are available. In our past work, we have focused on a class of conductivity models using Tikhonov regularization that exhibit smoothly varying properties. Thus we introduce a matrix \mathbf{W} , based upon a FD approximation to the Laplacian (∇^2) operator applied in Cartesian coordinates, to reduce model curvature in three dimensions. The influence of the smoothing constraint is controlled by the parameter λ . A common recipe for its selection is based upon a cooling approach (Haber & Oldenburg 1997). One carries out multiple solutions to the inverse problem starting with a large fixed value for λ . As λ is reduced, the data error, represented by the first term in eq. (1), will decrease. The process of reducing λ can then be repeated until the data error agrees with a target misfit based upon the assumed noise content of the data.

2.1 Non-linear conjugate gradient minimization

In large-scale non-linear problems, as considered here, we shall minimize (1) using gradient-based optimization techniques because of their minimal storage and computational requirements. We char-

acterize these methods as gradient-based techniques because they employ only first derivative information of the error functional in the minimization process. Gradient-based methods include steepest descent, non-linear conjugate gradient (NLCG) and limited memory quasi-Newton schemes. Newman & Boggs (2004) provide detail derivation of the gradients and an efficient scheme for their computation. Here, the focus is on a NLCG minimization approach because our past experiences have shown it to be the most efficient. The pre-conditioned NLCG algorithm we use in the minimization of eq. (1) is written as follows.

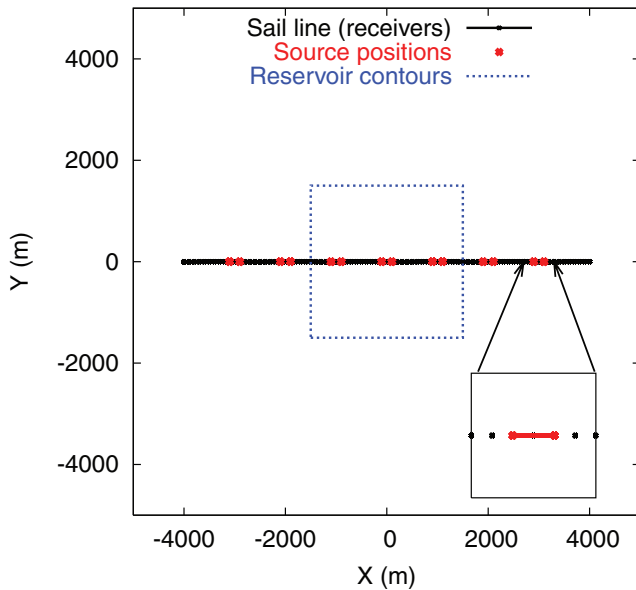
NLCG Algorithm

- (1) set $i = 1$, choose initial model \mathbf{m}_i and compute $\mathbf{r}_i = -\nabla\Phi(\mathbf{m}_i)$
- (2) set $\mathbf{u}_i = \mathbf{M}_i^{-1}\mathbf{r}_i$
- (3) perform line search to find α_i that minimizes $\Phi(\mathbf{m}_i + \alpha_i\mathbf{u}_i)$
- (4) set $\mathbf{m}_{i+1} = \mathbf{m}_i + \alpha_i\mathbf{u}_i$ and compute $\mathbf{r}_{i+1} = -\nabla\Phi(\mathbf{m}_{i+1})$
- (5) stop when $|\mathbf{r}_{i+1}| < \epsilon$, otherwise go to step 6
- (6) set $\beta_{i+1} = (\mathbf{r}_{i+1}^T\mathbf{M}_{i+1}^{-1}\mathbf{r}_{i+1} - \mathbf{r}_i^T\mathbf{M}_i^{-1}\mathbf{r}_i)/\mathbf{r}_i^T\mathbf{M}_i^{-1}\mathbf{r}_i$
- (7) set $\mathbf{u}_{i+1} = \mathbf{M}_{i+1}^{-1}\mathbf{r}_{i+1} + \beta_{i+1}\mathbf{u}_i$
- (8) set $i = i+1$ and go to step 3.

The matrix operator \mathbf{M}_i^{-1} in the algorithm is a pre-conditioner, which steers and scales the conjugate search direction \mathbf{u}_i such that it more closely approximates the Newton direction. A properly chosen pre-conditioner has a tremendous impact in accelerating the algorithm's convergence (Newman & Boggs 2004), however at a higher computational expense. To use the NLCG algorithm sensibly also requires efficient computation of the gradient \mathbf{r} . Sometimes, implementations of NLCG include a very accurate line search to ensure conjugacy. However, for the 3-D problems this is not practical because the evaluation of the error functional is very expensive. Moreover, conjugacy has little meaning in the non-linear and non-quadratic context. Instead, we have developed a procedure that gives an acceptable decrease of the functional with a minimal number of evaluations. Newman & Alumbaugh (2000) discuss the issue and show that it is possible to achieve acceptable decreases in the error functional using a line search based upon quadratic interpolation, safeguarded with back tracking. Usually, an additional forward modelling application per source, defined by a transmitter operating at a specific frequency, is all that is needed for the line search. This yields

Table 2. Computational times and resources needed for all inversions carried out in this work. Hardware specifications: Intel(R) Xeon(TM) CPU 3.60 GHz.

Inversion number	Number of CPUs ($n_x \times n_y \times n_z \times n_d$)	Iterations	Computing time per iteration (min)	Total computing time (hr)
1a (reference)	144 (3 × 4 × 4 × 3)	87	32.5	47.1
1b (coarse-grid)	144 (3 × 4 × 4 × 3)	97	5.1	8.2
2a (reference)	27 (3 × 3 × 3 × 1)	80	50.2	66.9
2b (coarse-grid)	27 (3 × 3 × 3 × 1)	75	1.3	1.6
3	100 (5 × 5 × 4 × 1)	250	4.7	20.0
4	64 (4 × 4 × 4 × 1)	150	0.6	1.6
5a	64 (4 × 4 × 4 × 1)	21	4.4	1.6
5b	64 (4 × 4 × 4 × 1)	24	15.4	6.2
5c	64 (4 × 4 × 4 × 1)	33	4.2	2.4
5d	64 (4 × 4 × 4 × 1)	58	21.7	21.0
6	128 (4 × 4 × 4 × 2)	172	19.8	56.7

**Figure 3.** Inversion 1: Transmitter–receiver configuration for synthetic data generation of a single-profile seafloor survey.

three forward modelling applications per source and per inversion iteration.

2.2 The forward problem

Minimization of eq. (1) involves the error functional gradient $\nabla\Phi$, that is, the derivative of Φ with respect to the model parameters in the vector \mathbf{m} . The data part of Φ and the predicted data \mathbf{d}^p are linked directly through the forward problem. It is described by the time harmonic Maxwell equations in the diffusive approximation,

$$\sigma \mathbf{E} - \nabla \times \mathbf{H} = -\mathbf{J} \quad (2)$$

$$\nabla \times \mathbf{E} + i\omega\mu_0 \mathbf{H} = -\mathbf{M}, \quad (3)$$

where a time dependence of $e^{i\omega t}$ is assumed ($i = \sqrt{-1}$). For CSEM applications, the typical range of the angular frequency ω allows us to neglect displacement currents.

Applied currents generate the electric and magnetic fields, \mathbf{E} and \mathbf{H} , and are denoted by \mathbf{J} and \mathbf{M} for electric and magnetic sources, respectively. The Earth's electrical conductivity σ is a function of position that is allowed to vary in three dimensions. On the other

hand, we set the magnetic permeability μ to its free space value μ_0 . Variations in the magnetic permeability are rare, and are usually confined to magnetic ores and some volcanic soils.

Our solution method for the forward modelling problem is based upon the consideration that the number of model parameters, required to simulate realistic 3-D geology, can typically exceed 10^7 . Finite difference modelling schemes are ideally suited for this task, because they can be parallelized to handle large-scale problems that cannot be easily treated otherwise (Alumbaugh *et al.* 1996). After approximating the Maxwell equations on a staggered grid (Yee 1966) at a specific angular frequency, using finite differencing and eliminating the magnetic field (Alumbaugh *et al.* 1996), we obtain a linear system for the electric field,

$$\mathbf{K}\mathbf{E} = \mathbf{S}, \quad (4)$$

where \mathbf{K} is a sparse complex symmetric matrix with 13 non-zero entries per row. The dimension of \mathbf{K} is $N_e \times N_e$, where N_e is the FD grid's total number of edges. Its diagonal entries depend explicitly on the electrical conductivity, σ . The conductivity distribution throughout the model space is to be estimated by the inversion process. Since the electric field, \mathbf{E} , also depends upon the conductivity, implicitly, this gives rise to the non-linearity of the inverse problem. The fields are sourced with a grounded wire or loop embedded within the modelling domain. The corresponding discrete source vector \mathbf{S} includes Dirichlet boundary conditions imposed upon the problem. To avoid excessive meshing near the source, we favour a scattered-field formulation to the forward problem. In this instance, \mathbf{E} is replaced with \mathbf{E}_s in eq. (4). The source term, for a given transmitter, will now depend upon the difference between the 3-D conductivity model and a simple background model, weighted by the background electric field, \mathbf{E}_b , where $\mathbf{E} = \mathbf{E}_b + \mathbf{E}_s$. We favor simple background models, such as whole space or layered half-space models that can be easily and rapidly simulated. Given the solution of the electric field in eq. (4), the magnetic field can be easily determined from a numerical implementation of Faraday's law,

$$\mathbf{H} = \frac{1}{-i\omega\mu_0} \nabla \times \mathbf{E}. \quad (5)$$

For realistic earth imaging, involving a large amount of data and hence many sources, a large number of solutions to eq. (4) follows. Consequently, an efficient solution process is paramount. We solve the forward problem to a predetermined error level using iterative Krylov subspace methods, using either a biconjugate gradient (BICG) or quasi-minimum residual (QMR) scheme with preconditioning (Alumbaugh *et al.* 1996). In general we employ the QMR method with a Jacobi pre-conditioner for marine CSEM type

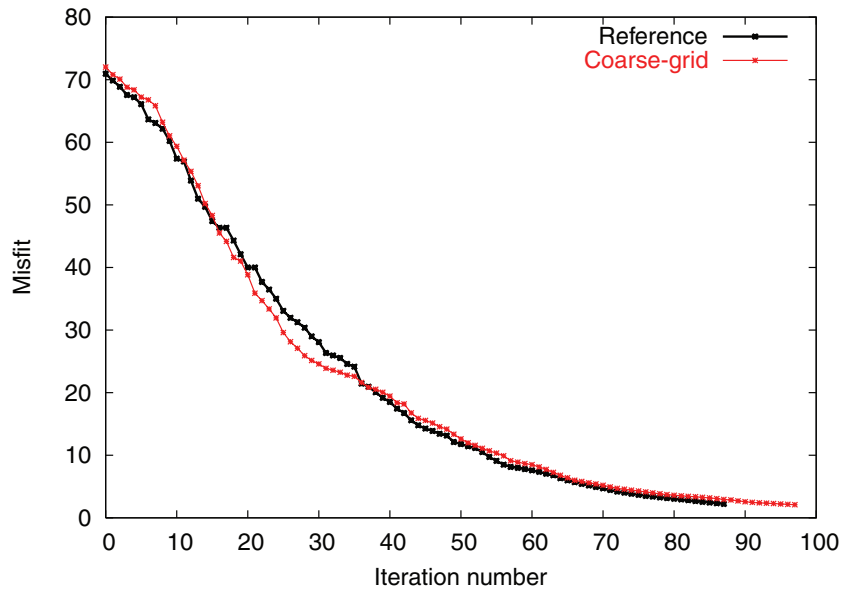


Figure 4. Inversion 1: Error functional Φ , according to eq. (1), of synthetic single-profile data inversion.

problems. More elaborate pre-conditioners have been tested and shown to be not that effective for this problem. These include simple Neumann and Least-Squares polynomials, incomplete Cholesky factorization, and algebraic multigrid (AMG) (Newman *et al.* 2004). The AMG scheme is the most elaborate of the pre-conditioners tested, and attempts to preserve the null space of the Maxwell operator through properly designed grid transfer operators. While this scheme can produce very fast solutions to the forward problem, it thus far has been found to be unstable for use with highly complex models. Another pre-conditioner considered has been found advantageous for low induction numbers (Newman & Alumbaugh 2002). This owes to the poor solution convergence, caused by a large null-space of the curl–curl operator contained in the matrix \mathbf{K} of eq. (4), as the field excitation frequency approaches the static limit. However, for the frequencies considered in this work, we expect relatively small solution time improvements, compared to the improvements achieved by optimized grids.

3 OPTIMIZATION OF THE SIMULATION MESH

We assign a conductivity parameter, $\sigma_k, k = 1, \dots, M$, to each cell of the model domain, where M equals the total number of model cells. In the following, the model grid is denoted by Ω_M . The subset $\Omega_m \subseteq \Omega_M$ shall represent the inversion domain, with m model unknowns. The parameter σ_k is real valued and collectively stored in the model vector $\mathbf{m} = \Sigma_M$, which is piecewise constant. Further, the finite-difference simulation grid Ω_S of size N_c , where N_c equals the number of FD mesh cells, is introduced. Both grids are Cartesian with conformal grid axes along the x, y , and z -directions. Usually, one has $\Omega_S = \Omega_M (N_c = M)$. For most cases within this work, the (computational) optimization involves coarser and/or smaller (in terms of grid extensions) simulation meshes, hence $N_c < M$.

The solution of the forward problem requires a conductivity mapping from Ω_M to Ω_S , that is, the computation of an effective conductivity on the edges of the FD mesh, where the electric fields \mathbf{E} are sampled. For a given 3-D mesh Ω_S we define the vector of

directional edge conductivities,

$$\begin{aligned} \Sigma_S &= (\sigma_1^x, \sigma_1^y, \sigma_1^z, \dots, \sigma_{i_c}^x, \sigma_{i_c}^y, \sigma_{i_c}^z, \dots, \sigma_{N_c}^x, \sigma_{N_c}^y, \sigma_{N_c}^z)^T \\ &= (\sigma_1^e, \dots, \sigma_{i_c}^e, \dots, \sigma_{N_c}^e)^T, \end{aligned}$$

for building the $N_e \times N_e$ FD stiffness matrix \mathbf{K} of the linear system (4). Note that N_c and N_e denote the total number of grid cells and edges, respectively, belonging to the grid Ω_S . To compute the edge conductivities, we introduce a linear mapping operator $\mathcal{M}_{N_e \times M}$,

$$\mathcal{M}(\Sigma_M) = \Sigma_S, \quad (\mathcal{M} : \Omega_M \rightarrow \Omega_S).$$

Consider a given edge i_e , belonging to the cell i_c of the FD mesh Ω_S , for the example of an edge along the x -axis. In the case $\Omega_M = \Omega_S$, the corresponding element of Σ_S is computed from

$$\sigma_{i_e}^e = \sigma_{i_c}^x = \sum_{i=1}^4 \sigma_i w_i, \quad w_i = \frac{dV_i}{\sum_{j=1}^4 dV_j}, \quad (6)$$

where w_i are weights determined by volume fractions. Fig. 1(a) shows that the four cell conductivities σ_i are given by the four model cells connected by the edge where $\sigma_{i_c}^x$ (red arrow) is sampled. These four adjoining cells describe a parallel circuit. Hence, each line of the matrix operator $\mathcal{M}_{N_e \times M}$ involves an arithmetic average of the form as in eq. (6). For the equal-grid case, its corresponding edge i_e thus has four non-zero entries $w_i = \frac{1}{4}$.

In the case $\Omega_M \neq \Omega_S$, we employ a material averaging scheme based on an integro-interpolation method mentioned by Moskowitz *et al.* (1999). In principle, the method allows to compute edge conductivities on the grid Ω_S from a series of parallel circuits on Ω_M . Moreover, there may exist an arbitrary translation, assuming conformal grid axes, between Ω_M and Ω_S . It can be seen that the example of eq. (6) represents a special case of the more general formulation

$$\sigma_{i_e}^e = \sigma_{i_c}^x = \left[\sum_{j=1}^J \left(\frac{1}{V_j} \sum_{i=1}^{I_j} \sigma_i dV_i \right)^{-1} \Delta x_j \right]^{-1} \Delta X_{i_c}, \quad (7)$$

where

- (i) ΔX_{i_c} = length of the edge i_e (here along the x -axis),
- (ii) J = number of discrete parallel circuits P_j along ΔX_{i_c} ,

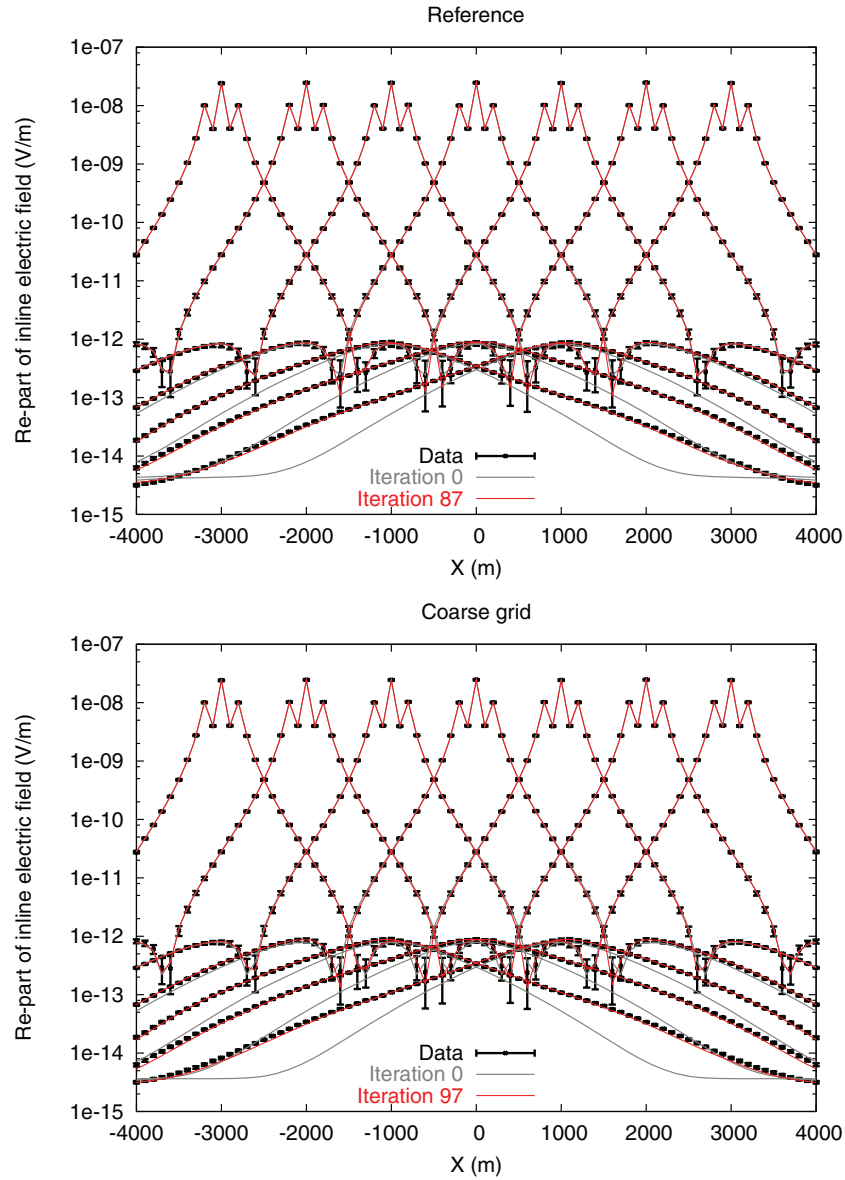


Figure 5. Inversion 1: Data fits for all seven sources (survey configuration shown in Fig. 3), exemplified for the excitation frequency $f = 0.25$ Hz. Initial (grey) and final fits (red) for both reference and coarse-grid inversions are shown.

- (iii) V_j = total volume of a discrete parallel circuit P_j ,
- (iv) I_j = number of model mesh cells included in the volume V_j or overlapped by V_j ,
- (v) dV_i = volume fraction of σ_i contributing to a parallel circuit P_j .
- (vi) Δx_j = segment length of the parallel circuit P_j (here along the x -axis).

In eq. (7), the inner arithmetic average produces the effective conductivity owing to a parallel circuit of the conductors σ_i . Further, the outer sum represents a serial integration of the parallel circuits along the total edge length ΔX_{i_c} , where $\sum_{j=1}^J \Delta x_j = \Delta X_{i_c}$. The averaging scheme is best illustrated in two dimensions. In Fig. 1(b), Ω_M and Ω_S are indicated by the black and red grid lines, respectively. For this case one has $J = 4$, $I_j = 2$ for all j , and the dependencies of P_j on the overlapped cells of Ω_M are: $P_1(\sigma_1, \sigma_4)$, $P_2(\sigma_2, \sigma_4)$, $P_3(\sigma_3, \sigma_4)$, $P_4(\sigma_3, \sigma_5)$. Each volume dV_i is given by the overlap of the integration area assigned to the edge $\sigma_{i_c}^x$ (shown in

pink) with the volume of the corresponding model cell σ_i . Note that $\sum_{i=1}^{I_j} dV_i = V_j$. Obviously, to obtain $\sigma_{i_c}^y$ and $\sigma_{i_c}^z$ for the 3-D case, this serial/parallel circuit integration is carried out along the y and z edges of the simulation grid cell i_c , respectively.

Since the inversion unknowns σ_k belong to Ω_m , a mapping from Ω_S to Ω_m is required for computation of the gradient vector \mathbf{r} in the NLCG algorithm. Consider the data component, $\nabla \Phi_d$, of the gradient, that is the term $-\nabla \Phi(\mathbf{m})$ involving only the first term of the right-hand side of eq. (1),

$$\nabla \Phi_d = -\text{Re}\{[\mathbf{D}\mathbf{J}]^T [\mathbf{D}(\mathbf{d}^o - \mathbf{d}^p)]^*\}.$$

Computing $\nabla \Phi_d$ implicitly requires the Jacobian, \mathbf{J} . Note, however, that we never form \mathbf{J} explicitly. Its elements are

$$J_{jk} = \frac{\partial d_j^p}{\partial \sigma_k}, \quad j = 1, \dots, N_d; \quad k = 1, \dots, M.$$

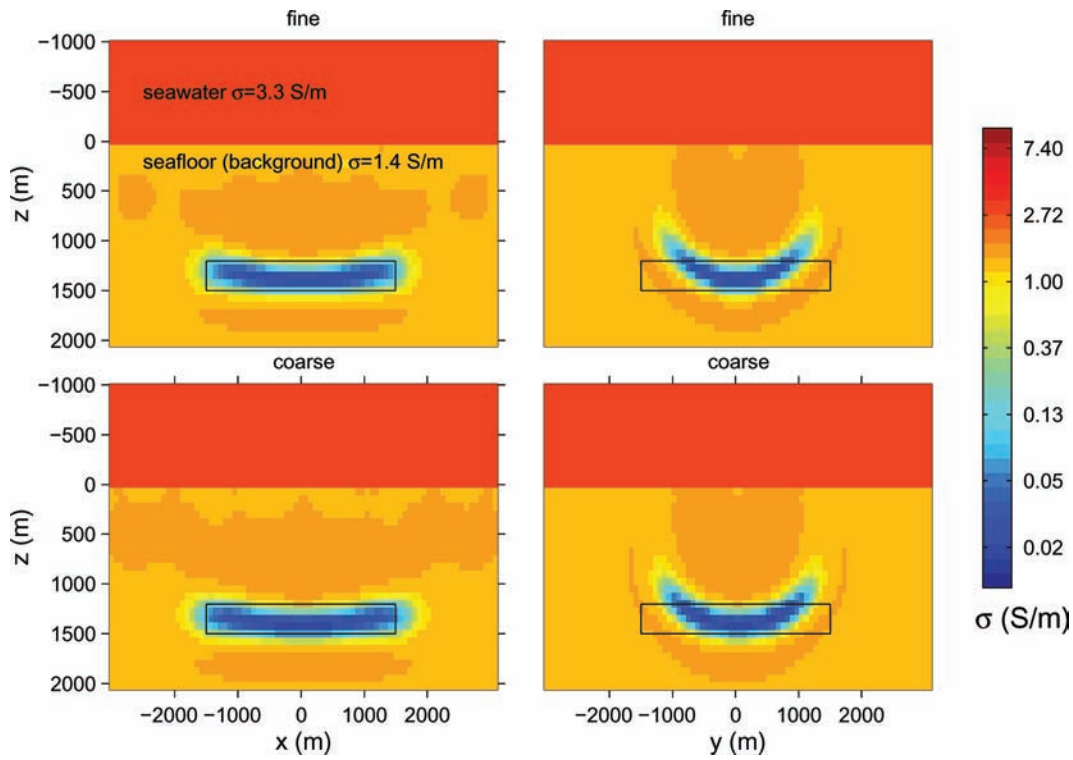


Figure 6. Inversion 1: Final model solution for reference (upper) and coarse-grid (lower) inversions.

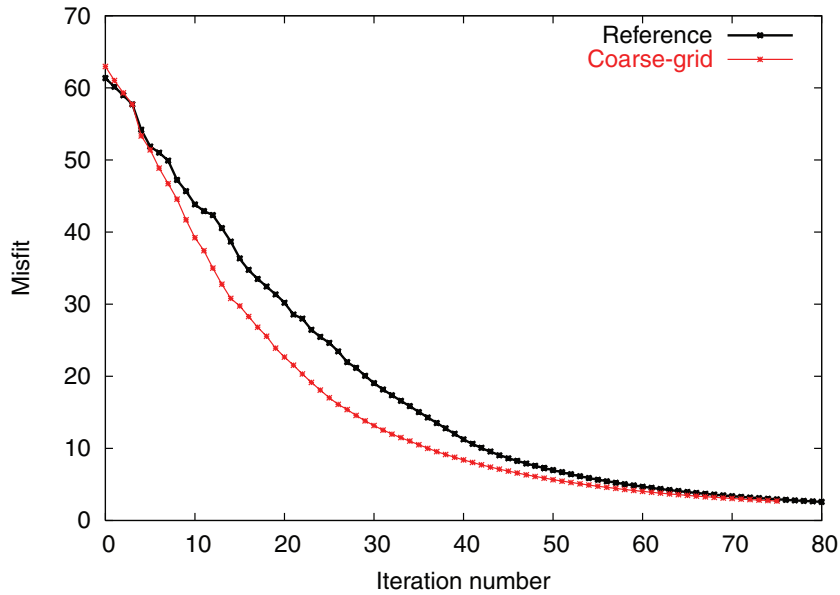


Figure 7. Inversion 2: Error functional Φ , according to eq. (1), of synthetic single-profile data inversion.

In terms of the electric field, a Jacobian element is defined by

$$J_{jk} = \mathbf{q}_j^T \frac{\partial \mathbf{E}}{\partial \sigma_k},$$

where \mathbf{q}_j is the j th column vector of a $N_d \times N_e$ ($N_d = \text{size of } \mathbf{d}^\circ$) interpolation operator, which maps the electric field solution \mathbf{E} from Ω_S onto the N_d detector locations defined on Ω_M . The data sensitivities $\frac{\partial \mathbf{E}}{\partial \sigma_k}$ follow from differentiating eq. (4) with respect to

the model unknowns σ_k (Newman & Hoversten 2000),

$$\frac{\partial \mathbf{E}}{\partial \sigma_k} = \mathbf{K}^{-1} \left(\frac{\partial \mathbf{S}}{\partial \sigma_k} - \frac{\partial \mathbf{K}}{\partial \sigma_k} \mathbf{E} \right). \quad (8)$$

Note that the term $\frac{\partial \mathbf{S}}{\partial \sigma_k}$ is non-zero/zero for a scattered/total field solution. The data sensitivity for the k th model parameter has non-zero entries for these edges i_e that have a contribution from σ_k through the average (7). In the case $\Omega_M = \Omega_S$, this amounts to 12 edge contributions, arising from the edges that define the boundaries of the model cell σ_k . In other words, as illustrated by the additional arrows

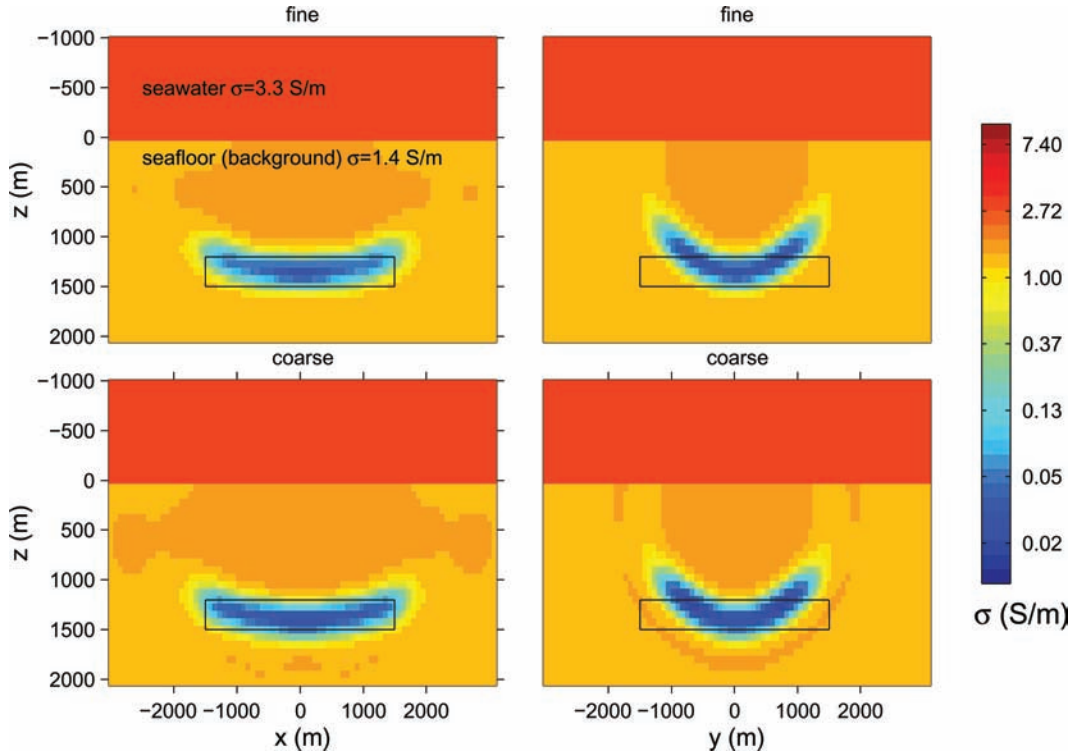


Figure 8. Inversion 2: Final model solution for reference (upper) and coarse-grid (lower) inversions.

in Fig. 1(a), there are four edge conductivities for each Cartesian direction, which depend on σ_k through their corresponding average exemplified by eq. (6). In the general case, we denote the number of edge contributions by $N_e(k)$. Then it follows from the chain rule

$$\frac{\partial \mathbf{K}}{\partial \sigma_k} = \sum_{n=1}^{N_e(k)} \frac{\partial \mathbf{K}}{\partial \sigma_n^e} \frac{\partial \sigma_n^e}{\partial \sigma_k}, \quad (9)$$

and a similar expression for $\frac{\partial \mathbf{S}}{\partial \sigma_k}$. The inner derivatives, $\frac{\partial \sigma_n^e}{\partial \sigma_k}$, of (9) are obtained from the derivative of eq. (7),

$$\frac{\partial \sigma_n^e}{\partial \sigma_k} = \frac{\sigma_n^{e2}}{\Delta X_{ic}} \sum_{j=1}^{J'} \Delta x_j \left(\frac{1}{V_j} \sum_{i=1}^{I_j} \sigma_i dV_i \right)^{-2} \frac{dV_k}{V_j}. \quad (10)$$

Here, $J' \leq J$ is the number of segments (parallel circuits $P_{j'}$) with a non-zero contribution from σ_k . For $\Omega_M = \Omega_S$, one has $J' = 1$, $\Delta x_{j'} = \Delta X_{ic}$, and hence $\frac{\partial \sigma_n^e}{\partial \sigma_k} = w_k$, which are the corresponding weighting coefficients of the simple average (eq. 6). The general case is again illustrated in two dimensions in Fig. 1(b). For this example, the model cell σ_4 (yellow rectangle) shall also correspond to the fourth model unknown ($k = 4$). Then eq. (10) becomes

$$\frac{\partial \sigma_n^x}{\partial \sigma_4} = \frac{\sigma_n^{x2}}{\Delta X_{ic}} \sum_{j=1}^3 \Delta x_j \left(\frac{1}{V_j} \sum_{i=1}^2 \sigma_i dV_i \right)^{-2} \frac{dV_4}{V_j}.$$

Here, $J' = 3$, because σ_4 contributes to the three parallel circuits $P_1(\sigma_1, \sigma_4)$, $P_2(\sigma_2, \sigma_4)$ and $P_3(\sigma_3, \sigma_4)$.

4 IMPLEMENTATION OF CONSTRAINTS

Implementation of constraints is helpful in reducing solution ambiguity in the imaging process and avoiding non-physical conductivity

estimates, that is, negative or unrealistically high conductivity estimates. Here, we consider box constraints to restrict the electrical conductivity within the imaging volume to be bounded. Specifically, one requires

$$a_k < m_k < b_k,$$

for the k th model parameter. Here, we consider box constraints to bound the electrical conductivity within the imaging volume. An active set method requires the model update to be strictly feasible. When components of the current model are on the bounds, the method checks the steepest descent direction to determine if the corresponding components of the pending model update will be no longer feasible. If this is the case, we deflate to zero those corresponding components in the search direction that will be used in the line search process to update the model. Hence, there will be no changes in these model components on the bounds during and after the update. On the other hand, if during the line search, a trial step shows that a bound would be violated, backtracking along the deflated search direction keeps the updated model strictly feasible. Implementation of an active set scheme to enforce bound constraints is straight forward, but may cause convergence degradation of the NLCG algorithm (Nocedal 1995).

An alternative involves usage of transformation functions that map the bounded conductivity parameters to an unbounded domain in the transform space. Our inversion scheme allows to choose between two such transformations. The first is an inverse hyperbolic tangent transformation and the second is based on log parameters. In effect, both schemes transform a constrained inverse problem to an unconstrained type. Similar types of transformations within multidimensional frequency- and time-domain inversion frameworks, based on logarithmic parameters, have been quite effective in insuring that the electrical conductivity is strictly positive (Newman & Alumbaugh 2000; Commer *et al.* 2006).

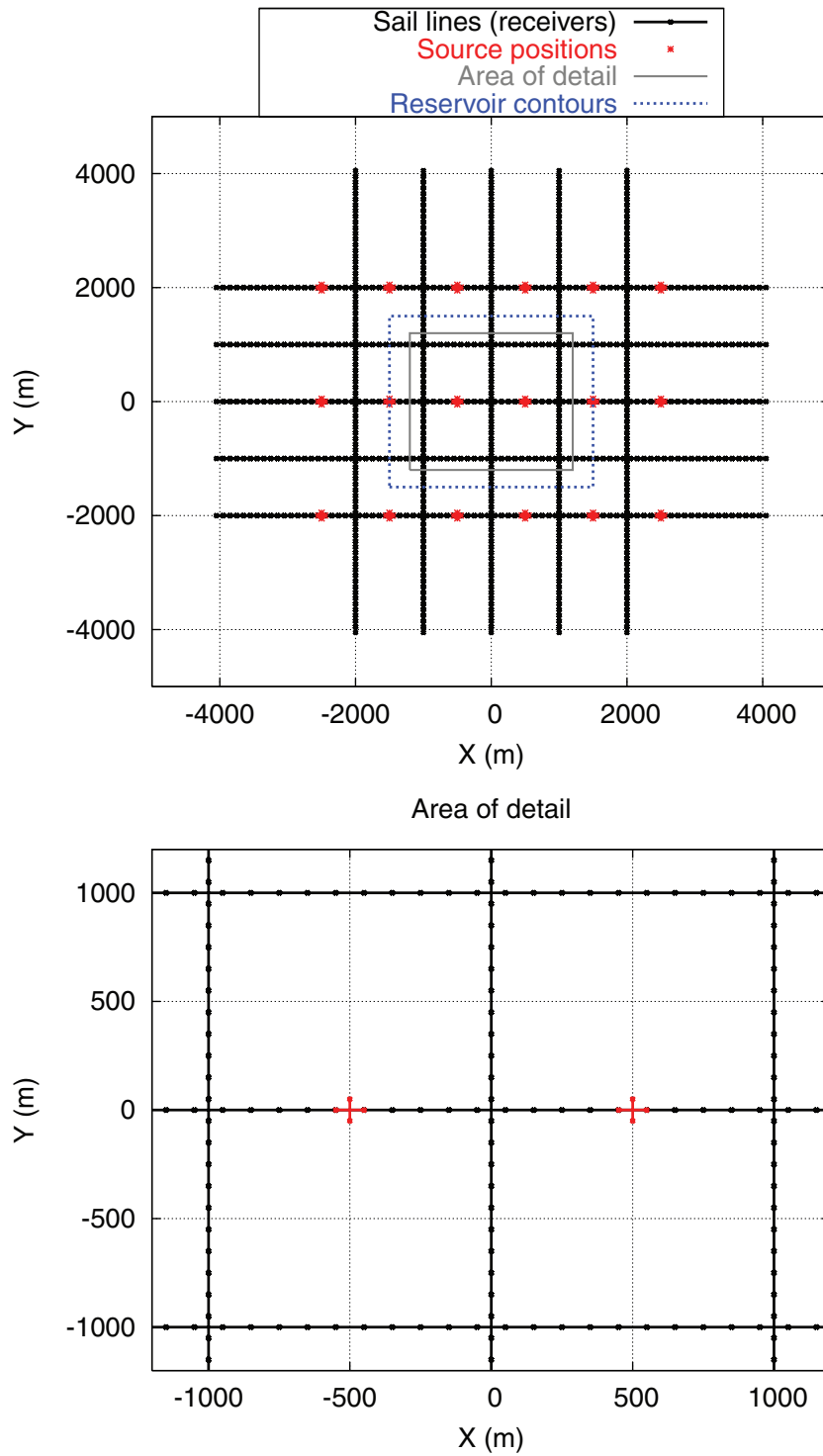


Figure 9. Inversion 3: Transmitter-receiver configuration of 3-D seafloor survey with grid layout.

Details of the transform method for enforcing upper and lower bounding constraints are as follows. Consider the first transformation where

$$m_k = \left(\frac{b_k - a_k}{2} \right) \tanh(x_k) + \left(\frac{b_k + a_k}{2} \right); \quad -\infty < x_k < \infty. \quad (11)$$

Here, x_k is the representation of the model component in the transform space, and $m_k = \sigma_k$. Further, the transformed parameter is

related to the original model parameter by the expression

$$x_k = \tanh^{-1} \left(\frac{2m_k - b_k - a_k}{b_k - a_k} \right); \quad a_k < m_k < b_k. \quad (12)$$

Differentiating eq. (11) with respect to x_k , utilizing eq. (12), yields

$$\frac{\partial m_k}{\partial x_k} = \left(\frac{b_k - a_k}{2} \right) \operatorname{sech}^2 \left[\tanh^{-1} \left(\frac{2m_k - b_k - a_k}{b_k - a_k} \right) \right]. \quad (13)$$

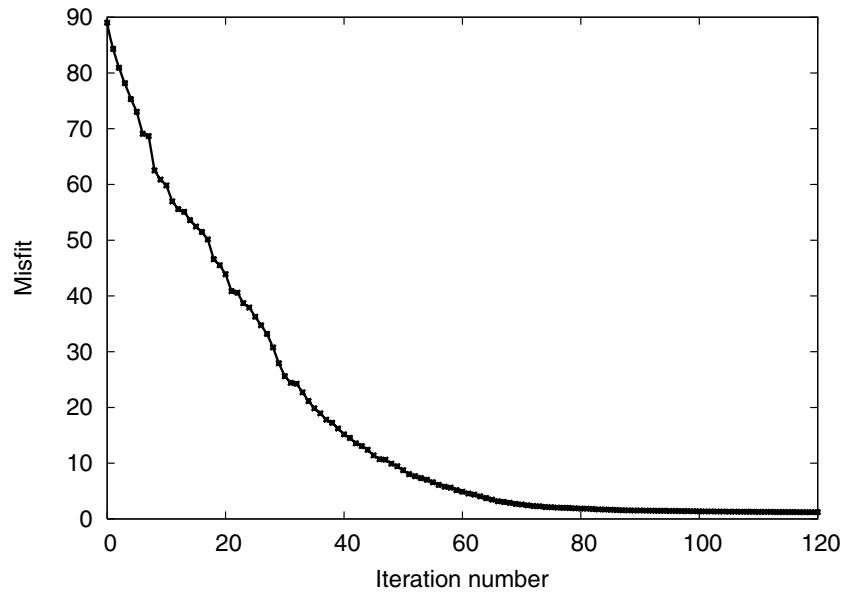


Figure 10. Inversion 3: Error functional Φ , according to eq. (1), of synthetic multiprofile data inversion.

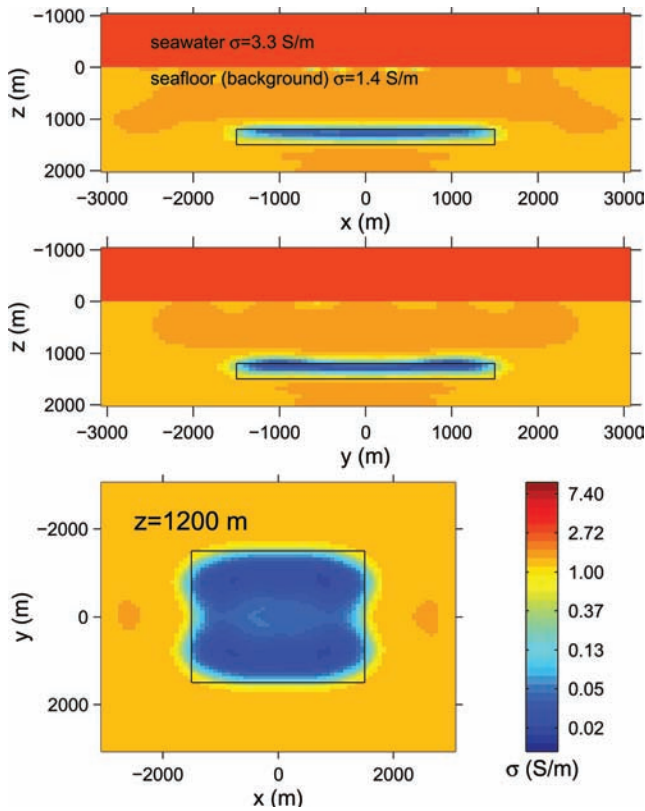


Figure 11. Inversion 3: Final model solution.

The hyperbolic secant function in eq. (13) is always positive and bounded and when squared is similar to a normal Gaussian distribution. It achieves its maximum value of $(b_k - a_k)/2$ when $m_k = (b_k + a_k)/2$.

For the second option of logarithmic parameters one has for the equivalent of eqs (11)–(13)

$$m_k = \frac{a_k + b_k \exp(x_k)}{1 + \exp(x_k)}; \quad -\infty < x_k < \infty. \quad (14)$$

Table 3. Inversion 4: endpoint positions (x, y, z) of transmitter dipole in metres for imaging study with source signature correction.

True (displaced) positions		Assumed positions	
Endpoint 1	Endpoint 2	Endpoint 1	Endpoint 2
-3100,0,0	-2900,-50,-50	-3100,0,0	-2900,0,0
-2100,0,-30	-1900,-20,0	-2100,0,0	-1900,0,0
-1100,-100,0	-900,-100,0	-1100,0,0	-900,0,0
0,0,0	200,0,0	-100,0,0	100,0,0
900,100,0	1100,0,-60	900,0,0	1100,0,0
1900,0,0	2000,0,-20	1900,0,0	2100,0,0
2900,-50,-20	3100,30,-70	2900,0,0	3100,0,0

$$x_k = \log(m_k - a_k) - \log(b_k - m_k); \quad a_k < m_k < b_k. \quad (15)$$

$$\frac{\partial m_k}{\partial x_k} = \frac{(b_k - a_k) \exp(x_k)}{[1 + \exp(x_k)]^2} \quad (16)$$

The graphs in Fig. 2 exemplify both transformation types. One can observe the linear behaviour of both transformation functions when the unbounded parameter has values in the vicinity of zero.

Using eq. (13) or (16), it is a simple matter to recast the cost functional gradient in terms of the transformed variable, where component wise we have

$$\frac{\partial \Phi}{\partial x_k} = \frac{\partial \Phi}{\partial m_k} \frac{\partial m_k}{\partial x_k} \quad (17)$$

Another advantage of this type of transformation is that it may produce sharper image rendering if tight bounds are selected from *a priori* information, as will be demonstrated in a synthetic example below. However, if the bounds are too restrictive, then it is possible that unacceptable data fits will result. With the transformed expression for the gradient in eq. (17), one can apply the NLCG algorithm directly to the transformed problem, which implicitly enforces the bound constraints. It is also understood that the regularization operator now applies directly to the transformed unknowns, $x_k (k = 1, \dots, m)$, in the minimization procedure.

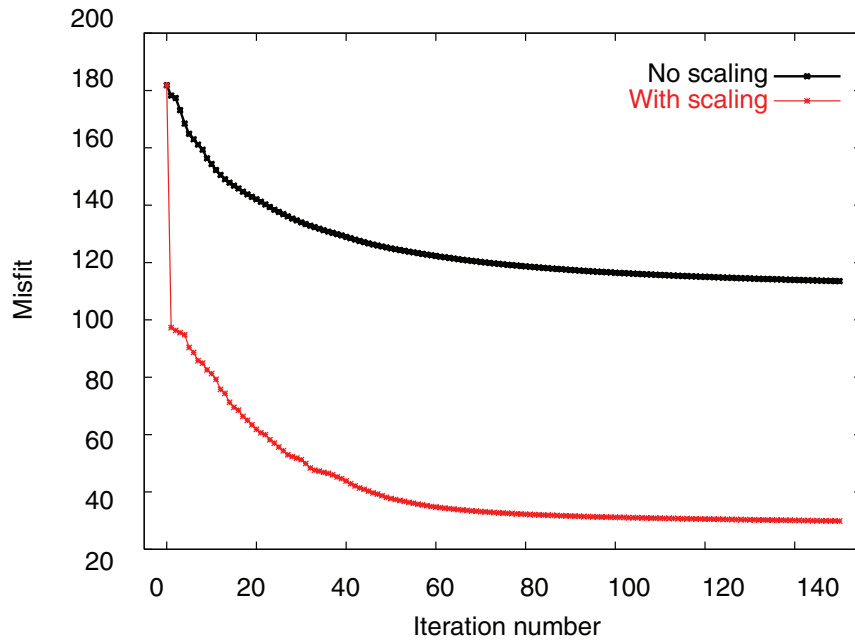


Figure 12. Inversion 4: Error functional Φ for data inversion without (black) and with (red) source signature correction factor.

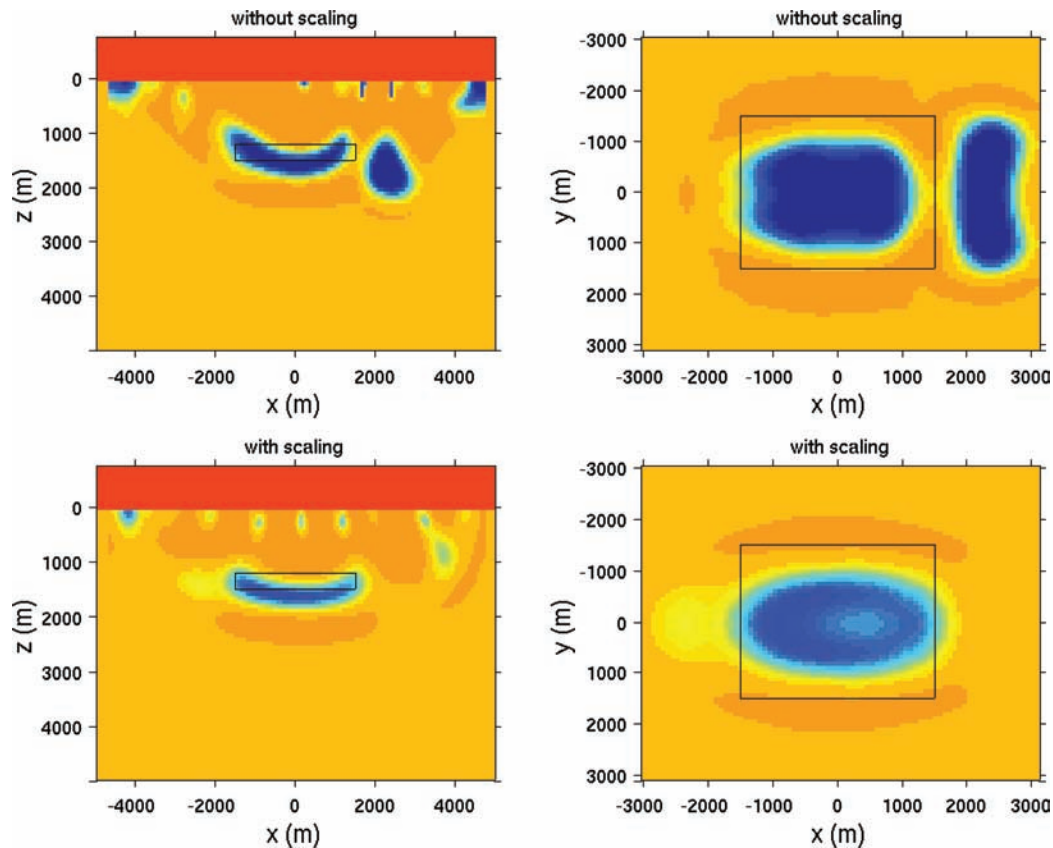


Figure 13. Inversion 4: Final model solution for inversion of data set with distorted transmitter endpoint positions. Upper/lower figures are created from inversions without/with source signature correction factor as an additional inversion parameter.

5 SOURCE SIGNATURE CORRECTION

In an inversion scenario with real field data, it is likely that data distortions due to systematic measurement errors vary with the

transmitter’s frequency. Moreover, each distinct source may be affected differently by positioning errors or local inhomogeneities in its vicinity that are not accounted for in a starting model. In time-domain forward modelling, such transmitter-characteristic data

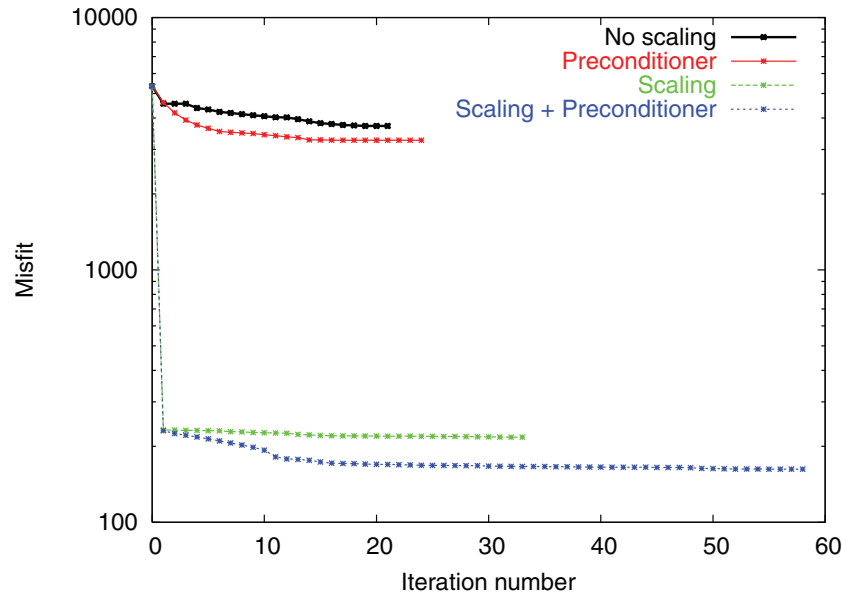


Figure 14. Inversion 5: Error functional Φ for inversion of distorted data without SSC factor and PC activated (black). Red, green, and blue curves show results when PC, SSC and both PC and SSC are active, respectively.

distortions can be taken into account by convolution of the modelling time curve with the Earth's impulse response measured nearby the transmitter. In the frequency domain, this translates to multiplication of the right-hand side of eq. (4) by a complex-valued scaling factor s ,

$$\mathbf{KE} = s\mathbf{S}. \quad (18)$$

Following the findings of Pratt (1999) for seismic waveform inversion, we found that it may be beneficial to assign an unknown complex scaling factor to each CSEM source, thus taking into account data distortions in the form of both amplitude and phase shifts. In an inversion framework, this is realized by augmenting the inversion parameters with a set of scaling factors, where one factor can be assigned to each distinct source or to multiple sources. Hence, one solves a source signature estimation problem together with the imaging problem by also minimizing the data part of eq. (1) with respect to s , where s is embedded within \mathbf{d}^p , leading to

$$s = \frac{\mathbf{d}^{oT} \mathbf{d}^{p*}}{\mathbf{d}^{pT} \mathbf{d}^{p*}}. \quad (19)$$

In practice, s is computed after each model update during an inversion iteration and applied to the modelling data \mathbf{d}^p afterwards.

An alternative way of addressing data distortions within an inversion framework would be the direct recovery via additional unknowns representing transmitter characteristics. This leads to the need of solving a problem that occurs in optimal experimental design. Generally, optimal experimental design aims at identifying experimental conditions, including sampling schemes, that deliver measurement data which are most sensitive to unknown parameters. Applying this concept to data distortions due to erroneous transmitter characteristics, one would first have to identify the types of transmitter characteristics that are in question. Compared to the simplicity of the method proposed here, such a scheme may become much more complicated, and thus shall not be investigated further within this work. As demonstrated below, the source signature correction may be helpful in certain scenarios. However, it shall be emphasized that a careful data pre-processing remains essential for optimal imaging results.

6 EXPLOITATION OF SOLUTION PARALLELISM

In a real industrial-sized data application, up to hundreds to thousands of transmitters might have to be employed, in order to image the subsurface at a sufficient level of spatial resolution and detail for mapping reservoirs (Carazzone *et al.* 2005). This can lead to tens of thousands of solutions to the forward modelling problem for a single imaging experiment. Hence, the computational demands for solving the 3-D inverse problem are enormous and non-trivial. To cope with this problem, our algorithm utilizes two levels of parallelization, one over the modelling domain, and the other over the data volume. All processor communication is carried out using the Message Passing Interface (MPI) software library.

6.1 Model decomposition

In solving the forward problem on a distributed environment, we first split up the FD modelling domain, not the matrix, into a Cartesian topology. The details of this scheme are outlined by Alumbaugh *et al.* (1996). Thus a forward modelling problem is solved amongst a number of $N_{xyz} = n_x \times n_y \times n_z$ processors. As the linear system is relaxed, which involves matrix-vector products on each of the N_{xyz} processors, values of the solution vector at the current Krylov iteration, that are not stored on the processor, must be passed by neighbouring processors to complete the product. In addition to this message passing between neighbouring processors, several global communications are carried out to complete the dot products needed for the Krylov relaxation iterations. The solution time's rate of decrease using this kind of parallelization flattens with increasing N_{xyz} , since the overhead due to message passing becomes more and more dominating.

6.2 Data decomposition

To avoid a message passing overhead, a second level of parallelization is realized by distributing the data, that is, the transmitters

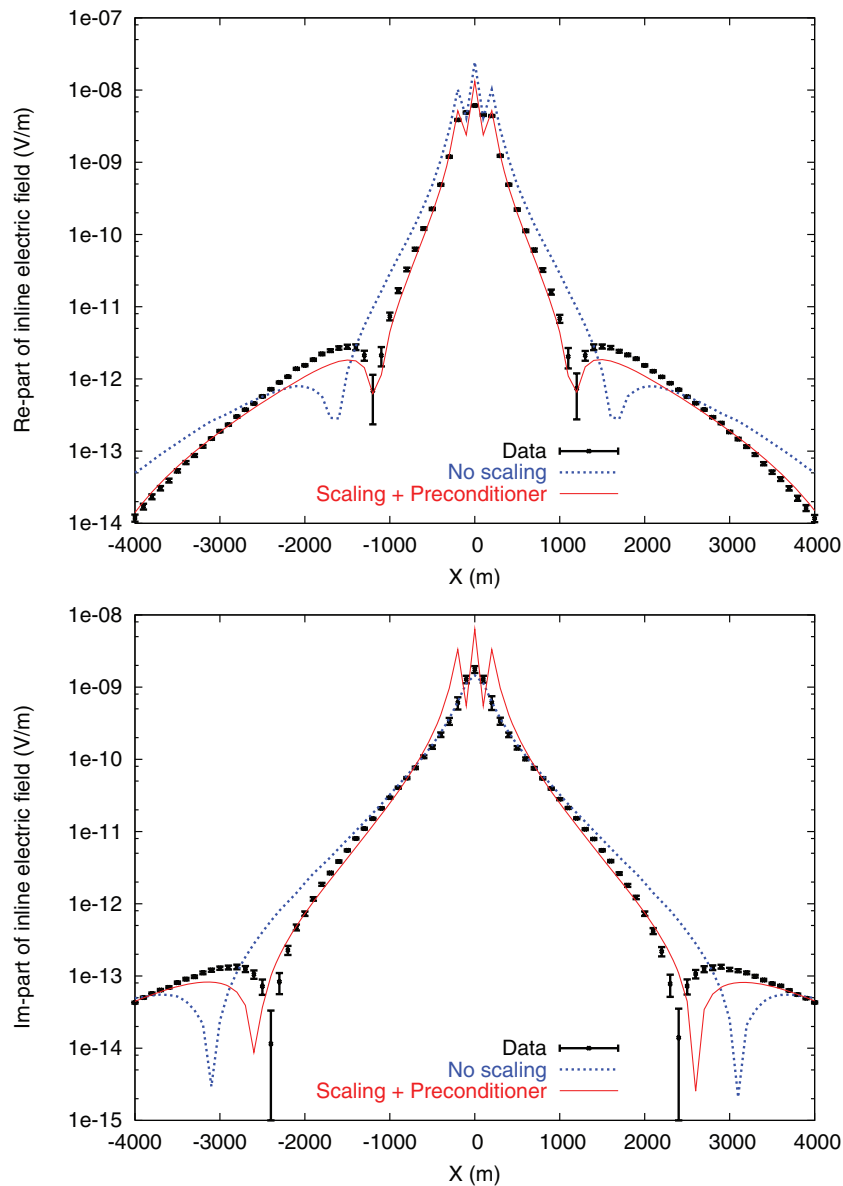


Figure 15. Inversion 5: Data fits exemplified for the source centred at $x = 0$ m of the survey configuration shown in Fig. 3. The excitation frequency is $f = 0.25$ Hz. The inverted data is given by the black symbols. Data computed from the inversion result are shown for the case without using SSC (blue) and for the case using both SSC and PC (red).

of a data set, over groups of processors. With a number N_{data} of such processor or data groups, one has thus a total number of tasks $N_{\text{total}} = N_{\text{xyz}} \times N_{\text{data}}$. This allows to keep a balanced ratio between N_{xyz} and the size of the forward problem, which is dictated by the size of its corresponding FD mesh Ω_s . At the same time, an arbitrarily large number of CPUs can be employed, as the number of data groups, N_{data} , can be increased linearly with the total number of transmitters employed in the imaging experiment.

One is interested in achieving maximum load balancing among the processor groups assigned to each data group, because global communication to compute dot products needs to be done several times per inversion iteration. Consider a set of transmitters where source–receiver configurations and source excitation frequencies vary. First, optimized FD meshes for this set may vary considerably in size, that is, the number of grid nodes. Second, convergence of the Krylov solutions are prone to deteriorate with high model con-

ductivity contrasts and, unless special pre-conditioning techniques are used, low excitation frequencies. Hence, bottlenecks may arise from large Krylov convergence differences between data groups. To achieve good load balancing, the transmitters are distributed among the data groups such that each group has a similar workload in terms of Krylov convergences. These can be estimated in advance from a trial inversion iteration. However, it shall be noted that convergence characteristics are subject to changes during later stages of an inversion, owing to changing model properties. In this work, all grid sizes are similar for the shown examples. Thus, we make the workload distribution dependable only on the transmitter frequencies, while N_{xyz} is kept constant for each data group.

The data decomposition is highly parallel. The main computational burden occurs with the forward FD solves. We have achieved nearly perfect scaling with this scheme. Provided sufficient computational capacity, it allows for realistic data sizes and 3-D imaging

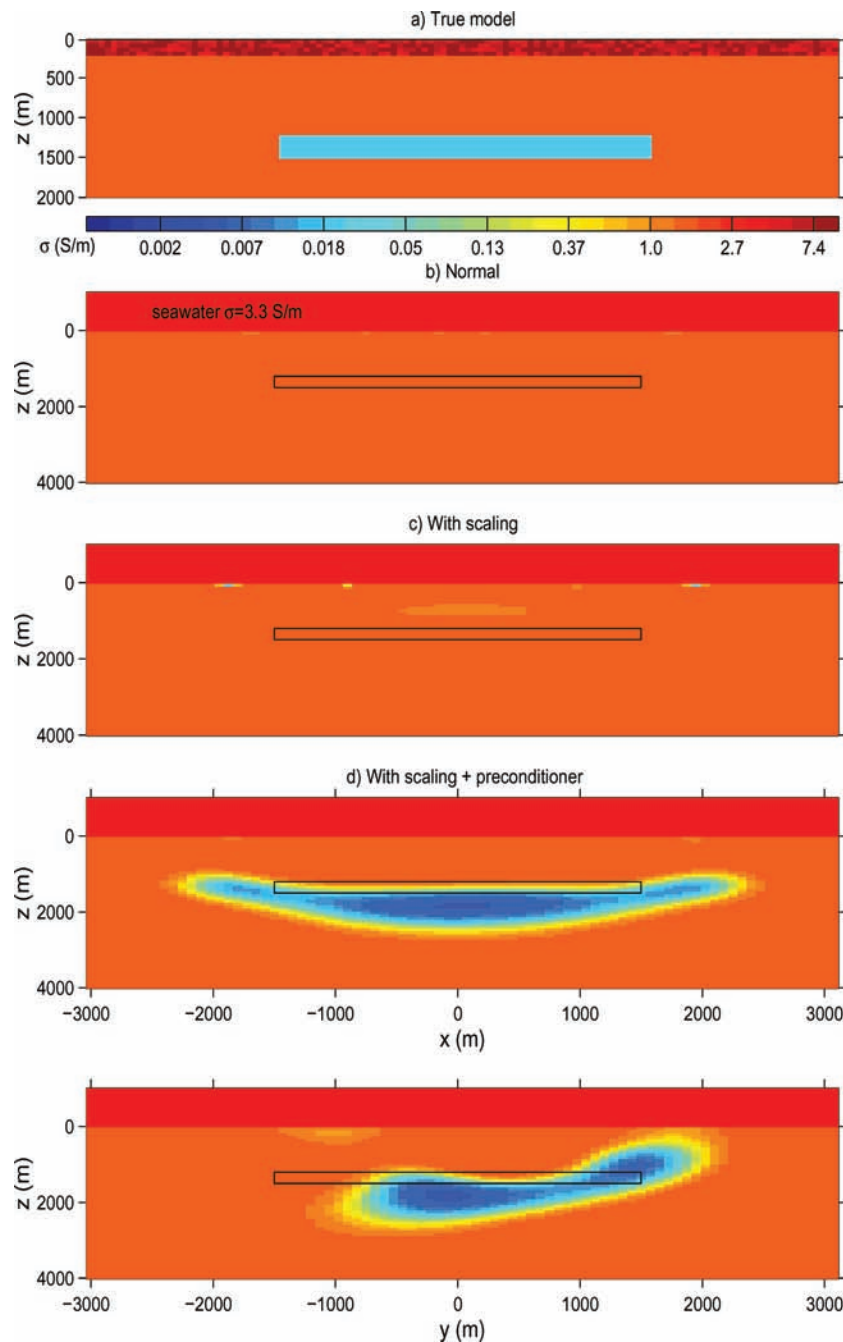


Figure 16. Inversion 5: (a) The inverted data set was created from a seabed model including a conductive upper layer of 200 m thickness with a randomly distributed conductivity between 4 and 10 S m^{-1} . (b) Inversion 5a: No pre-conditioner (PC) and no source signature correction (SSC) enabled. (c) Inversion 5c: Without PC, but SSC activated. (d) Inversion 5d: With both PC and SSC enabled, showing a strongly enhanced image at depth. Shown are both xz and yz sections.

volumes to be analysed on time scales acceptable to the exploration process.

7 SYNTHETIC MARINE CSEM SURVEY EXAMPLES

Synthetic inversion examples using data from a simulated marine environment are presented. The model consists of a resistive reser-

voir ($\sigma = 0.02 \text{ S m}^{-1}$) of size $3 \times 3 \times 0.3 \text{ km}$ along the x , y and z coordinates, respectively. The target is embedded into a homogeneous and conductive background ($\sigma = 1.4 \text{ S m}^{-1}$) and its upper boundary lies at a depth of $z = 1200 \text{ m}$ below the seafloor ($z = 0 \text{ m}$). Inversion results of different transmitter-receiver configurations will be shown below. Synthetic electric field data for the frequencies 0.25, 0.75 and 1.25 Hz were generated. Normally distributive Gaussian noise was added to the data, based upon three percent of the measurement amplitude. In addition, any data below

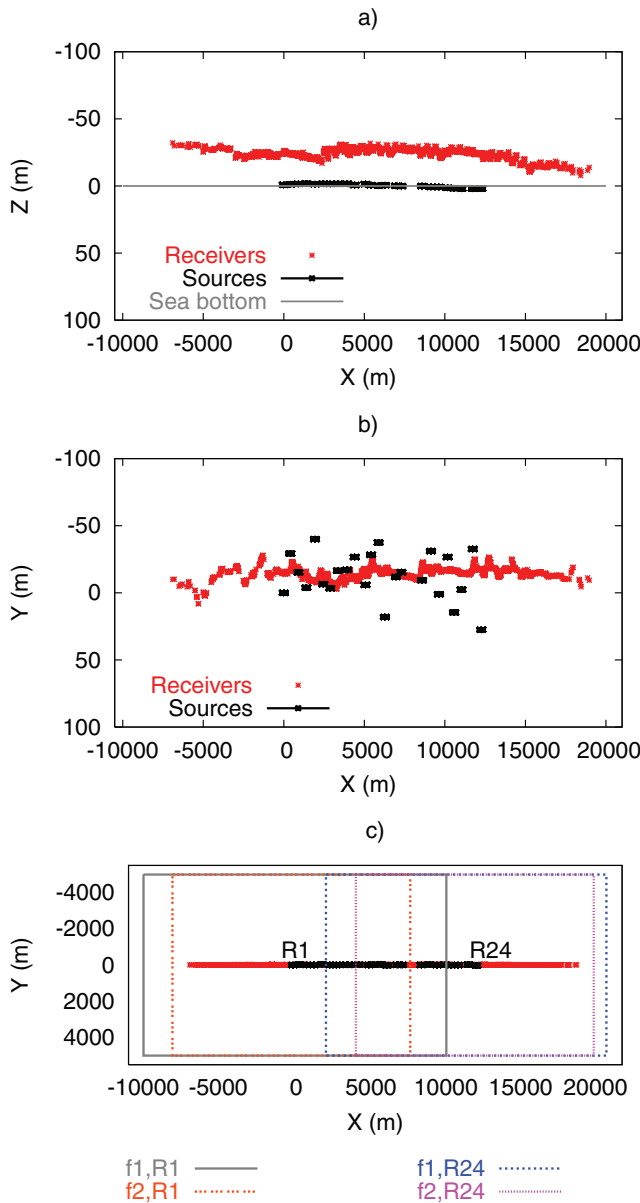


Figure 17. Layout of the survey over the Troll West Gas Province. (a) Vertical section (xz). (b) Horizontal section (xy). (c) Illustration of the model subdomains covered by the simulation grids assigned to sources R1 and R24 for both frequencies f_1 and f_2 .

Table 4. List of model and simulation grids for TWGP data inversion.

Grid	Number of cells	Δ_x	Δ_y	Δ_z	f (Hz)
Ω_M	$125 \times 41 \times 59$	250	250	100	
		$\Delta_x^{\min}/\Delta_x^{\max}$	$\Delta_y^{\min}/\Delta_y^{\max}$	$\Delta_z^{\min}/\Delta_z^{\max}$	
Ω_S^1	$85 \times 41 \times 85$	125/250	250/250	25/200	0.25 (f_1)
Ω_S^2	$110 \times 43 \times 85$	75/125	125/250	25/200	0.75 (f_2)

an assumed noise floor of $1 \times 10^{-13} \text{ V m}^{-1}$ were discarded from the analysis.

For this scenario, we design a rather conservative model grid Ω_M with a uniform node spacing of $\Delta = 75 \text{ m}$ and a size of $M = 134 \times 134 \times 134$ cells. This spacing fulfils a typical spatial sampling

requirement of 5 grid nodes per skin depth δ , where

$$\delta \approx 503 \sqrt{\frac{1}{\sigma_b f}} \quad (20)$$

is estimated using the seafloor background conductivity ($\sigma_b = 1.4 \text{ S m}^{-1}$) and the highest employed frequency, $f_3 = 1.25 \text{ Hz}$.

The inversion domain Ω_m covers 90 per cent of the model space below the seafloor. Because the CSEM data are generated from the same forward solution used in the inversion, we have taken steps to insure that the simulated data have some degree of independence from Ω_m . Specifically, a finer mesh, Ω_M^0 , with a node spacing $\Delta = 50 \text{ m}$, and thus a size of $M = 200 \times 200 \times 200$ cells, was used as FD simulation grid for data generation. The three simulation grids Ω_S employed in the inversions each have a uniform grid node spacing, which is adapted to the source frequency using eq. (20). For each grid, the grid spacing Δ is chosen to meet a spatial sampling requirement of 4 nodes per skin depth δ . Table 1 summarizes the details of all grids. The main purpose of the synthetic data inversions presented here is a feasibility study for adaptive simulation meshes. Therefore, we choose a rather ideal starting model with the true background conductivity for all inversions.

In the following, each imaging experiment shall be numbered consecutively. Refer to Table 2 for computational requirements of each inversion.

7.1 Inversion 1: Single profile, three frequencies

The configuration of the first synthetic imaging study, referred to as Inversion 1, is shown in Fig. 3. A single profile with seven inline horizontal electric dipole transmitters runs across the target's centre, where each source has a length of 200 m and is located at $z = 0 \text{ m}$. Note that we have applied the reciprocity principle to the synthetic data. The positions of the real CSEM transmitter along the sail line become the computational receiver positions, and the real CSEM detectors on the seafloor become computational sources. Therefore, sources and receivers refer to the computational sources and receivers as they are defined in the simulations. The electric point dipole receivers are located at $z = -50 \text{ m}$ and are separated by a distance of 100 m. Only inline electric fields are inverted, which are the fields parallel to the transmitter orientation. Each source operates at the three frequencies $f_1 = 0.25 \text{ Hz}$, $f_2 = 0.75 \text{ Hz}$ and $f_3 = 1.25 \text{ Hz}$. Hence, computation of the predicted data at each inversion iteration effectively requires 21 forward solutions. We refer to the inversions using the coarser simulation meshes as coarse-grid inversions. For a comparison, a reference inversion result (number 1a in Table 2) was also produced, where $\Omega_S^i = \Omega_M$ for all three frequencies f_i . Further, a logarithmic type of parameter transformation according to eq. (15) with constant lower/upper bounds of $0.005/1.5 \text{ S m}^{-1}$ is employed.

For both inversions, the total error functional, computed from eq. (1), is depicted in Fig. 4. Data fits are exemplified for the frequency $f_1 = 0.25 \text{ Hz}$ in Fig. 5. The reference and coarse-grid inversions needed 87 and 97 iterations, respectively, to reach a final data misfit of one. Refer to Table 2 (Inversions 1a,b) for details about the computational resources used for these results. While the coarser meshes enable a computational speed-up factor of 5.5, the final image shows no significant deterioration, compared to the reference inversion, as can be seen in Fig. 6.

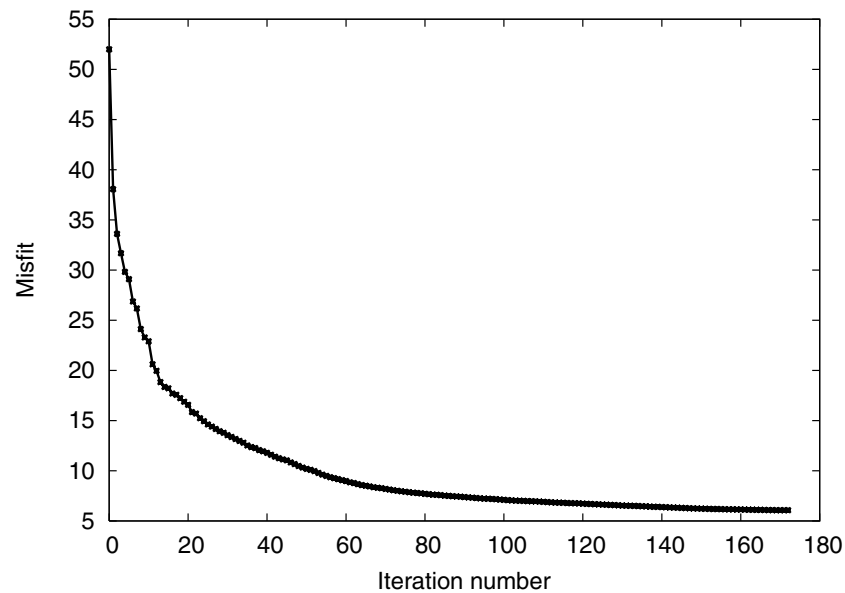


Figure 18. Error functional Φ of the TWGP inversion.

7.2 Inversion 2: Single profile, one frequency

In a typical imaging experiment, one might want to start inverting a subset of the data in order to refine an image in a step-by-step fashion. In the next study (Inversion 2a,b), we demonstrate that for the kind of target chosen here, the data of the lowest frequency, $f_1 = 0.25$ Hz (seven sources), provides sufficient information for resolution of the conductor at depth. Error functional and final model are shown in Figs 7 and 8. This inversion produces an image very similar to the previous one, however with a slightly less pronounced resistor.

Because both inversions 1 and 2 only employ a single sail line, one observes limited lateral sensitivity perpendicular to the sail line. While the resolution along the profile is satisfactory for this target, the lateral sensitivity to the target is limited to ± 1 km along the y direction. The bow-shaped lateral image (‘migration smile’) also results from a lack of resolution. Obviously, the lateral geometry of the target that can be recovered will be highly dependent on the survey coverage. Hence, high resolution 3-D imaging of marine CSEM measurements will require spatially exhaustive data volumes such as those generated by multiple sail lines over the target.

7.3 Inversion 3: Grid layout, one frequency

A third imaging study (Inversion 3) uses data from 10 profiles in a grid layout shown in Fig. 9. Here, the profiles contain altogether 18 source locations, where each location has two horizontal source polarizations. In contrast to the previous inversions, the receiver dipoles have two endpoints and a length of 100 m. We invert only the data of the frequency $f_1 = 0.25$ Hz. In total, the data set contains 36 effective sources and 14 442 data points. A total number of 120 inversion iterations are required to achieve the target misfit of 1.0 (Fig. 10). In a preliminary study, we observed very similar results between reference and coarse-grid inversions for such a profile layout. Here, only the coarse-grid result, using grid Ω_S^1 , is shown in Fig. 11. The generally sharp image indicates a highly improved lateral resolution, when comparing with the single-profile results. Instead of running a (fine-grid) reference inversion for the same number of

iterations, only the preliminary stage of the inversion was repeated using $\Omega_S = \Omega_M$; thereby we can estimate a computational speed-up factor of approximately 40 for this example.

For marine CSEM imaging experiments, thus far, the lower and upper bounding constraints promise to be very useful in alleviating conductivity overshoots (Gibbs phenomenon) near structural boundaries. We have also made the experience that, in contrast to unbounded parameters, both types of parametrizations are more powerful in suppressing near-surface image artefacts due to statics and positioning errors at the detectors. Though the shown synthetic studies demonstrate that acceptable models can be recovered, solution non-uniqueness remains a formidable problem. While employing both upper and lower bounding constraints can be highly beneficial, a convergence failure may result from too restrictive bounds. It is therefore, imperative that prior information be incorporated in the imaging process to restrict the class of solutions to geologically meaningful ones.

7.4 Inversion 4: SSC for positioning errors

For the following inversion study, we simulate a case where the measured positions of the real detectors on the seafloor would have errors. The source signature correction (SSC) factor shall be employed to alleviate the negative effects of positioning errors. We use the same data-generating model as in the previous examples, and a source–receiver configuration similar to that of inversion 2, with seven sources and a transmitter frequency of $f_1 = 0.25$ Hz. For creation of the distorted input data, the endpoint positions of the computational sources are modified according to Table 3. The two left columns list the true endpoints used for the synthetic data generation, and the two right columns are the (erroneous) positions as assumed for the inverted data. Two inversions were carried out, one without activating the source signature factor, another one with a separate factor s for each of the seven sources. Figs 12 and 13 show the error functional and the resulting images for both inversions. Comparing the results, it can be observed that there is significant improvement achieved by enabling the source scaling. While both model images exhibit the resistive target, additional artefacts, with

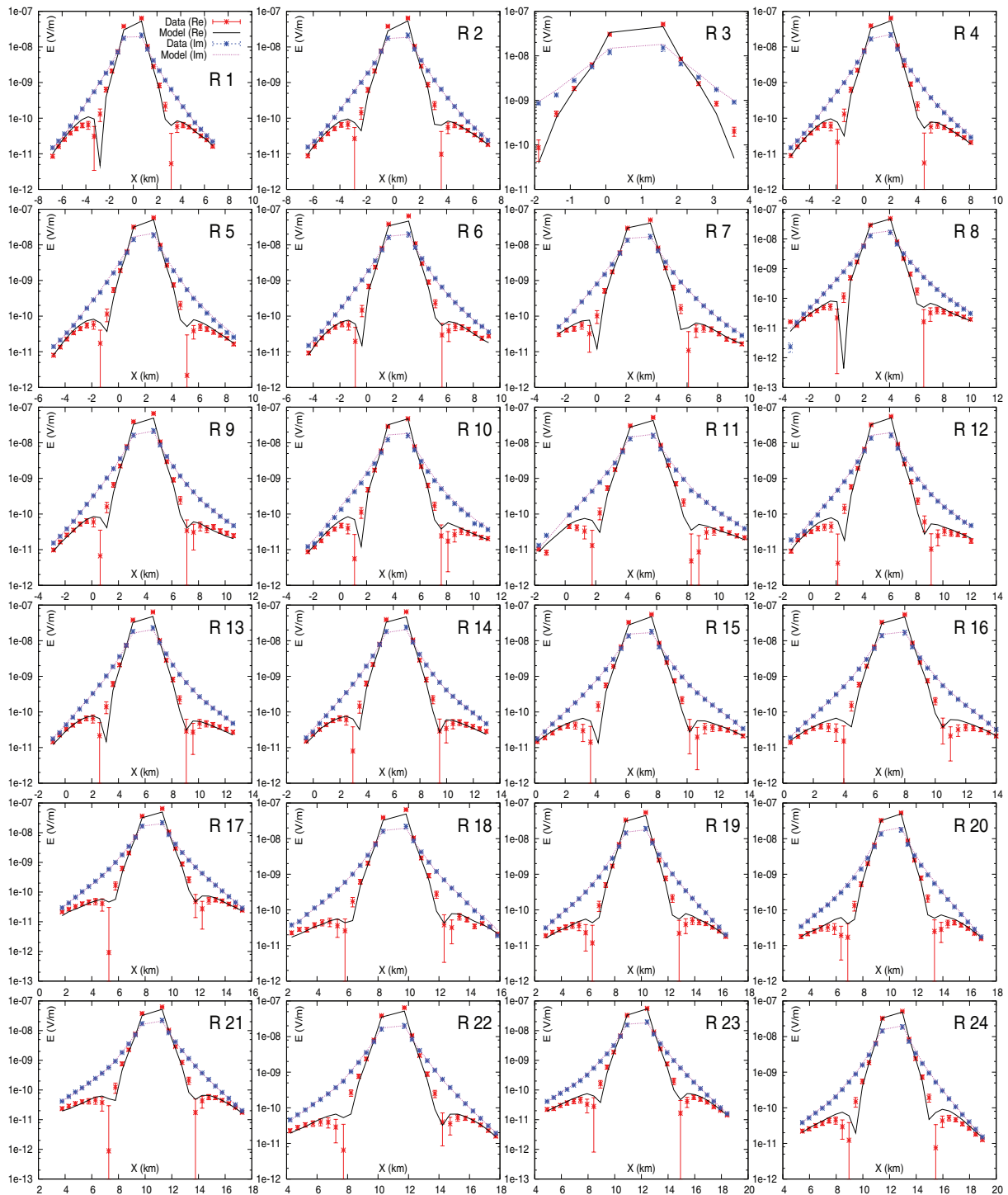


Figure 19. Data fits for TWGP inversion. Shown are observed and reproduced electric fields along the receiver profile for each source R1–R24 using the transmitter frequency $f_1 = 0.25$ Hz. The red and black curves are the real parts of the observed and reproduced electric field, respectively. The blue and purple curves are the corresponding imaginary parts.

the largest one nearly as large in size as the target, result from the inversion without scaling. The occurrence of artefacts is strongly suppressed when enabling the scaling factor. However, the convergence of the error functional towards a value of 27 indicates that the relatively large distortion imposed on the data can only be mitigated to a limited degree by the complex scaling factor.

7.5 Inversion 5: SSC for highly conductive overburden

In the next example, it is demonstrated for a different kind of data distortion, how the source signature correction factor may improve the inversion result. To generate strong data distortions, a layer with randomly distributed conductivities between 4 and 10 $S\ m^{-1}$ was

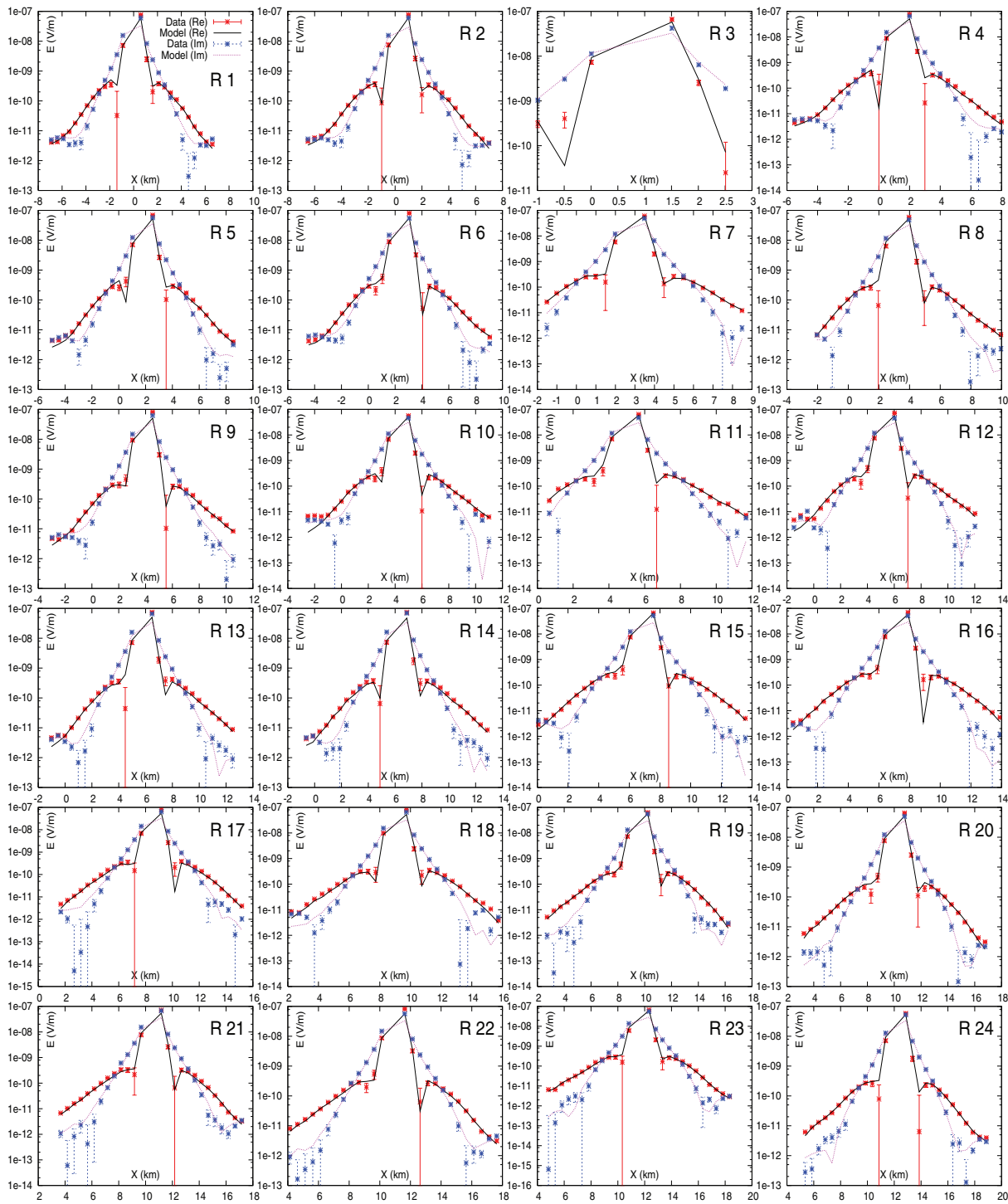


Figure 20. Data fits for TWGP inversion. Shown are observed and reproduced electric fields (real and imaginary parts) for each source R1–R24 using the transmitter frequency $f_2 = 0.75$ Hz.

added to the true model used for our synthetic data. The layer starts below the sea bottom and has a thickness of 200 m. As a starting model, a homogeneous background is assumed, again with the true conductivity. Here, we use the same survey layout, number of sources and frequencies, and (coarse) grids as for Inversion 1b. To see the effect of the SSC, two inversions (numbered 5a,b) without its activation are first carried out. The difference between these two inversions is that the second one uses a solution pre-conditioner

(PC). Key to this enhanced solution approach is an adjoint method that allows for an economical approximation of the Hessian used as the pre-conditioner \mathbf{M} for the NLCG algorithm (see Section 2.1). The matrix operation \mathbf{M}_i^{-1} in the algorithm is a PC, that changes the conjugate search direction \mathbf{u}_i such that it steers more towards the Newton direction. The effect of using the PC is that it scales the search direction, causing the activation of deeper regions in the model, that is, the inversion tends to put more weight on the

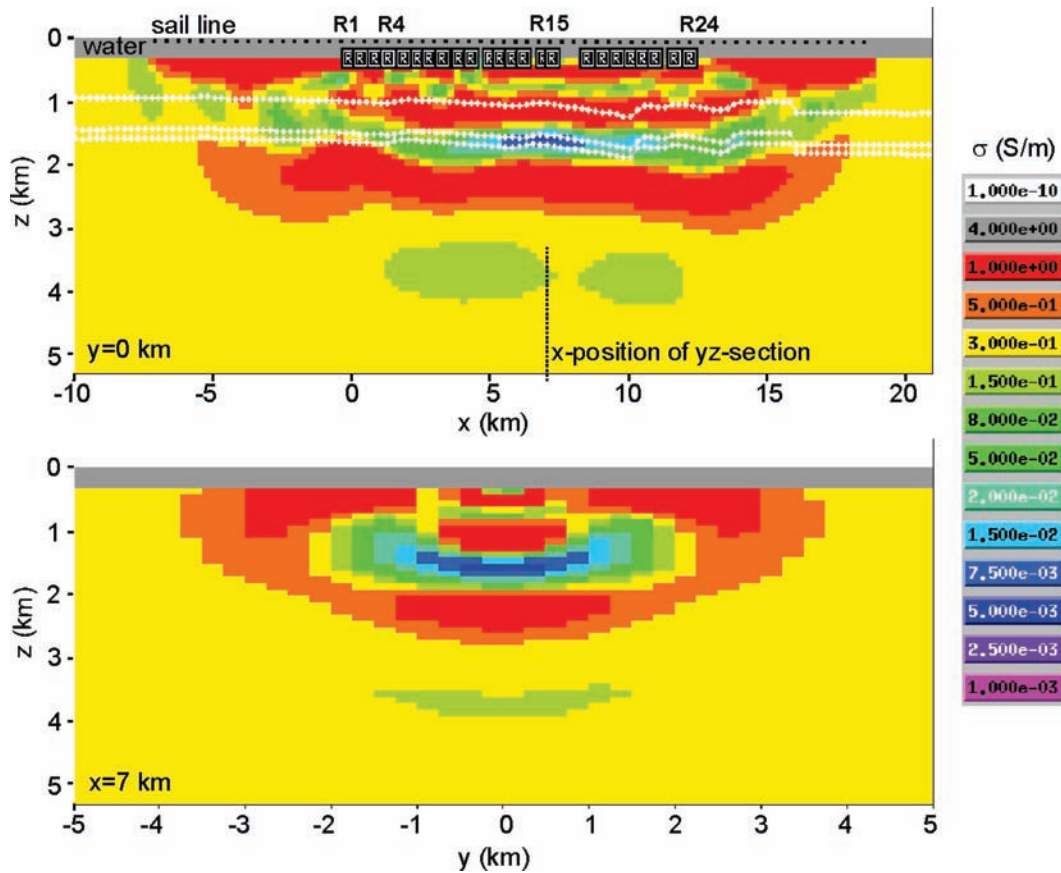


Figure 21. Final imaging result of TWGP inversion. R1–R24 mark the source positions projected to the xz -plane. The white lines in the upper figure represent interpreted seismic reflection horizons (Hoversten *et al.* 2006).

updates of the corresponding model components σ_k , compared to more shallow model regions. For more details about this type of PC the reader is referred to the work of Newman & Boggs (2004).

In addition to the two inversions without SSC, two more (numbered 5c,d) were carried out. The third one has the SSC activated, and the fourth one has both the SSC and PC activated. The error functional curves of all four attempts are shown in Fig. 14. Only the two inversions with SSC achieve a significant misfit decrease, where the pre-conditioned one reaches a final misfit which is by a factor of 1.3 smaller. Fig. 15 exemplifies the improved data fits for the source positioned at $x = 0$ m (see Fig. 3) and the excitation frequency $f_1 = 0.25$ Hz. The greatly improved data fits using the SSC also reflects in the final images shown in Fig. 16. The upper figure (a) shows the true model with the upper conductive seabed. Below (b) is the result obtained without using the SSC, where both the non-preconditioned and pre-conditioned inversions produce similar images. No resistive target appears in these images. Using the scaling factor (c), the resistor appears very faintly a few hundred metres above the true target. A strong yet distorted image of the reservoir is obtained when using both SSC and PC (d, two bottom graphs).

Although great solution improvement is achieved by using the SSC in a pre-conditioned inversion, one would have to exercise caution when interpreting the image. First, it has to be repeated that the strong data distortions simulated here can only be represented partly by the source signature. Second, the activation of deeper model regions by the PC may be stronger than desired. We note that the shown results using the SSC is a rather exploratory study, demonstrating its potential of solution improvement. Further studies with different

types of systematic data errors, which are typical in CSEM surveys, are to be carried out to gain further understanding about usage of EM source signatures in inversions.

8 FIELD DATA EXAMPLE

We present a field example using seabed logging data from the Troll West Gas Province (TWGP). This hydrocarbon reservoir is part of the large Troll Field complex, located offshore Norway. Details about the exploration site are given by Gray (1987), and the CSEM survey is outlined in detail by Johansen *et al.* (2005). Here, we give a summary about both the survey and the reservoir characteristics.

8.1 Survey and target

The survey layout, illustrated in Fig. 17 (a and b), comprises 24 CSEM detectors on a single profile, covering a profile length of approximately 12 km. The transmitter antenna is a horizontal electric dipole of length 230 m. It was towed along an overflight profile, at an average of 25 m above the detectors, covering a profile length of more than 25 km across TWGP. Within the Troll Field complex, the sea water depth varies between 300 and 360 m. The reservoir is embedded within Jurassic sandstones, where water bearing sands and overburden sediments have conductivities between 0.5 and 2 S m⁻¹. Resistivity measurements in an exploration well showed an average of 200–500 Ω m within the hydrocarbon bearing layer, and a maximum reservoir thickness of 160 m. The upper

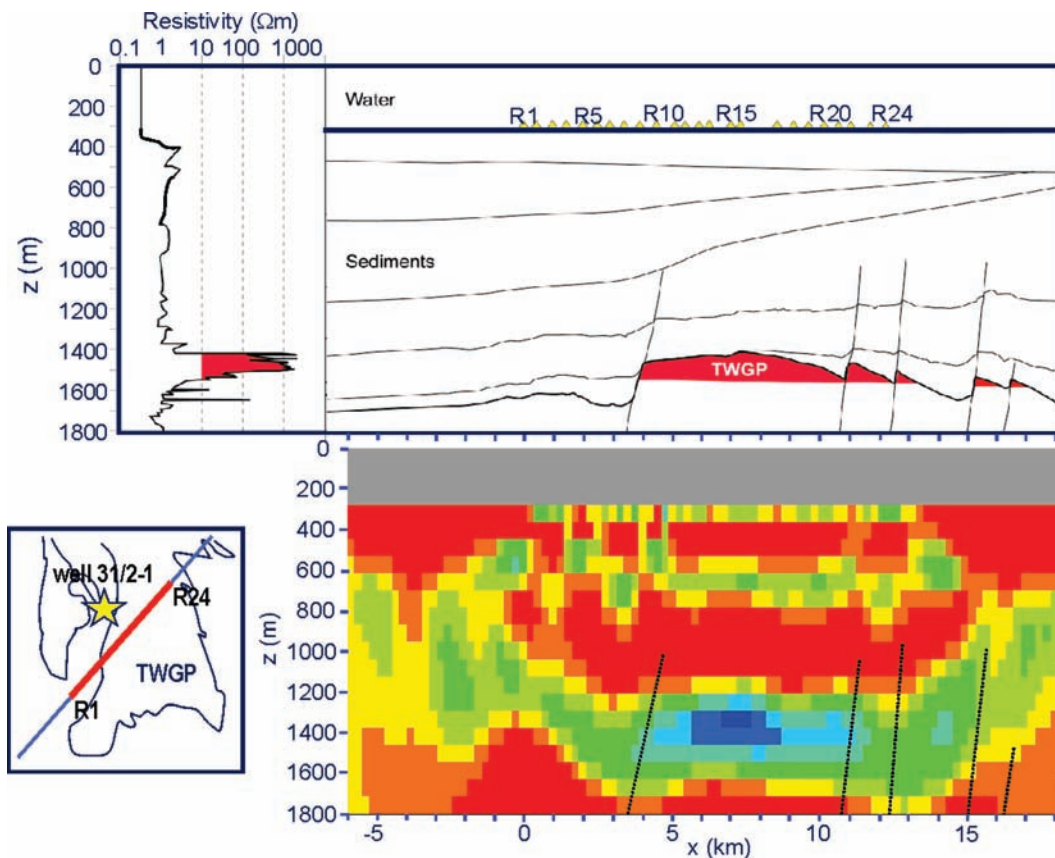


Figure 22. Comparison of inversion result with a simplified geological section across TWGP by Johansen *et al.* (2005). The geological section also includes the resistivity data from exploration well 31/2-1, which is located off the profile.

reservoir boundary's depth is about 1400 m below sea level ($z = 0$ m), with a horizontal extension of approximately 8 km along the survey profile.

In the following, the reciprocity principle is used again by changing the tow line of the real CSEM transmitter to the computational receiver profile, and the real detector positions to the computational sources. The inverted data set includes a total of 48 computational sources, operating at the two frequencies $f_1 = 0.25$ Hz and $f_2 = 0.75$ Hz, with 24 sources per frequency. The measurements consist of inline, that is, parallel to the source orientation, electric fields, these are 1192 data points in total. The survey also included measurements at a transmitter frequency of 1.25 Hz. The noise content of the data increases with the transmitter frequency. Inverting only the data belonging to the frequency f_1 , we were able to reach a final misfit of $\Phi = 1$. Adding data of the higher frequencies, the misfit converges towards a higher value. Compared to the two lower frequencies, the noise content of the data belonging to the frequency 1.25 Hz is relatively high. Hence, we decided to exclude this data from the inverted data set.

8.2 Inversion setup and result

In a preliminary modelling study, similar to the one outlined by Johansen *et al.* (2005), we found that bathymetry effects are negligible compared to the relatively large reservoir response. The maximum vertical difference between the source positions is 4 m over a source profile of more than 12 km. Therefore, our starting model contains a flat seabed with an averaged water depth of 323 m. All

sources are placed on the seabed at $z = 323$ m, while the original receiver positions with respect to the sources are kept. We use a starting model with a homogeneous background of 0.3 S m^{-1} below the sea bottom. No further *a priori* information is utilized during the inversion. Uniform model smoothing is applied within the whole inversion domain, using a regularization parameter of $\lambda = 0.1$. Because of the large target size, no bathymetry, and a rather moderate background conductivity variation within the model, a rather coarse modelling mesh can be used.

Again, the design of a proper modelling mesh and simulation meshes for both employed frequencies is based on skin depth estimations, as outlined in Section 7. All mesh details are summarized in Table 4. While the simulation grid stretching, with the minimum and maximum cell sizes also given in Table 4, is the same for all sources of the same frequency, a separate simulation mesh is assigned to each source in practice. Each simulation grid's node positions can thus be adapted to the source and receiver positions and their corresponding offsets. This is illustrated in Fig. 17(c) for the sources R1/R24 located on the left/right end of the source profile. The simulation grids assigned to these sources cover a different subset of the modelling mesh. Because of different skin depth criteria, the grids Ω_S^2 ($f_2 = 0.75$ Hz) cover a slightly smaller volume than Ω_S^1 ($f_1 = 0.25$ Hz).

We stopped the inversion (given number 6 in Table 2) after 172 iterations, when no more significant progress was made in the misfit decrease, shown in Fig. 18. The final data fits for both the real and imaginary parts of the electric field are shown in Fig. 19 for the frequency $f_1 = 0.25$ Hz and in Fig. 20 for $f_2 = 0.75$ Hz. Fig. 21 shows both xz and yz sections of the final image. The inversion

Table 5. Inversion 5: Comparison of the separate data misfits for all stations produced by the final TWGP solution and a non-reservoir model. For the non-reservoir model, all model cells within the reservoir region with $\sigma \leq 0.01 \text{ S m}^{-1}$ were set to $\sigma = 0.3 \text{ S m}^{-1}$.

Station	$f_1 = 0.25 \text{ Hz}$		$f_2 = 0.75 \text{ Hz}$	
	Reservoir	No reservoir	Reservoir	No reservoir
R1	2.5	6.6	4.7	35.5
R2	2.3	3.2	5.1	12.0
R3	5.8	3.9	5.1	5.1
R4	1.9	71.4	5.4	25.7
R5	3.6	6.3	6.5	43.8
R6	2.5	16.7	5.1	28.9
R7	2.0	116.7	5.8	24.7
R8	6.5	28.2	7.1	45.9
R9	2.0	15.3	5.6	34.1
R10	8.2	18.1	15.3	40.3
R11	4.2	86.3	13.1	39.7
R12	4.3	15.1	14.1	42.2
R13	1.9	13.3	7.5	52.4
R14	2.1	13.6	8.2	56.0
R15	2.3	17.4	3.7	56.7
R16	2.5	21.4	5.3	61.7
R17	1.9	12.5	8.6	67.1
R18	3.4	14.4	20.6	56.6
R19	1.9	13.1	6.0	50.9
R20	4.4	13.0	4.7	43.0
R21	1.5	12.6	6.4	46.9
R22	1.9	16.8	5.1	41.6
R23	2.3	13.3	4.4	57.2
R24	3.4	13.3	4.8	51.2

reaches a satisfactory data fit, produced from a model with a clear image of the resistive target. It was further found that inverting the data with the SSC activated does not improve the image in terms of delineating the reservoir zone. Hence, we consider the data quality as high enough.

A common way of incorporating prior model information would be the removal of the smoothing constraints, given by the second term in eq. (1), along surfaces identified as seismic horizons (Hoversten *et al.* 2006). This is based on the assumption that sharp changes in the acoustic impedance across reflection horizons also constitute layer boundaries with contrasting electrical conductivities. Although we did not incorporate such sharp boundaries into the smoothing constraints, both the depth and location of the reservoir is well within the boundaries defined by two seismic horizons, which were available as prior information, shown by the white lines in the xz -section of Fig. 21. Similar to the observations in the model result of inversions 1 and 2, the lateral resolution is limited along the single survey profile. However, the yz -section of the image also supports the large reservoir widths of 3.5–5 km assumed by Johansen *et al.* (2005).

8.3 Inversion solution analysis

It follows a comparison of the inversion result with a simplified geological model by Johansen *et al.* (2005), shown in Fig. 22. The geological section in the upper figure was based on 3-D FD forward modelling, and the incorporation of seismic reflection data and borehole EM measurements. Due to the diffusive nature of the EM fields, the CSEM method cannot clearly delineate the sedimentary layer boundaries. However, a resistive zone in the region $z = 500\text{--}750 \text{ m}$, embedded between two conductive layers, is indicated by our result. Below the reservoir, it is assumed that the high poros-

ity sands are filled with brine. The presence of such a brine layer is clearly indicated in the model by increased conductivities starting below a depth of 1700 m (Fig. 21). The image's background structure has also been indicated by other different inversion approaches (Hoversten *et al.* 2006). The image further shows conductivity variations in the shallow zone right below the seabed. From our experience with field data inversions, we assume that such variations arise when the inversion method attempts to compensate for both positioning errors in the data and/or a local variability in the seabed conductivity, which is not captured by the model discretization, including bathymetry effects. However, in this case the shallow variations are no major problem, because the primary purpose of the imaging experiment is the detectability of the resistive reservoir.

Comparing the geological section of Fig. 22 with the image shows a good match for the horizontal reservoir position. The reservoir top appears around $z = 1300 \text{ m}$ below sea level, while the well log data indicates a depth of $z = 1400 \text{ m}$. Note, however, that the well is a few kilometres away from the profile. In view of the fact that no sharp-boundary horizons were enforced in the inversion, the image shows a remarkably similar reservoir shape. It shall also be noted that the image contains relatively strong resistivity changes along the profile direction beyond the reservoir flanks. Although rather speculative, these patterns may be attributed to the vertical fault lines which were identified from the seismic information. These faults are indicated around the profile positions $x = 3, 11, 12, 15$ and 16 km in Fig. 22.

To investigate how relevant the reservoir is for fitting the data, a non-reservoir model was created from the final inversion result. The non-reservoir model has the background conductivity structure of the image, yet with the reservoir masked. In practice, all model cell conductivities $\sigma \leq 0.01 \text{ S m}^{-1}$ within the volume defined by $x = 4$ to 12 km , $y = -1$ to -1 km and $z = 1100$ to 1400 m are set to $\sigma = 0.3 \text{ S m}^{-1}$ (background conductivity of the starting model). Table 5 shows the separate data parts of the error functional Φ , given by the first term on the right-hand side of eq. (1). One data set is given by the source at one of the positions R1–R24, the source frequency, and the data points assigned to this source. Averaged over all 48 data sets, the data misfit increases by a factor of 8 when masking the reservoir. The total misfit, calculated by summing the misfit over all 1192 data points, is 33.5, compared to 5.2 for the reservoir model. Fig. 23 further exemplifies this difference. Shown are both real and imaginary field components for the data assigned to the sources R4, f_1 and R15, f_2 .

9 CONCLUSIONS

We have made significant progress in further reducing the computationally high demands of large-scale CSEM inverse problems. Being able to separate the simulation space from the model space, in terms of FD grid design, opens a range of possibilities. As demonstrated, a simulation mesh can be adapted to the source excitation frequency, source–receiver offsets, and its corresponding largest distances, and thus be optimized computationally. Depending on the location of a source in the model and its coverage of the inversion domain, given by the source–receiver geometry, the simulation mesh position can be optimized individually for each different source. As shown in the field data example, one can thus let the simulation grids assigned to a survey profile ‘slide’ along the profile, where they only have the minimum required grid sizes. Such a capability is essential for treatment of industrial field data sets, where survey profiles cover areas which may easily exceed sizes of 100 km^2 . The computation times

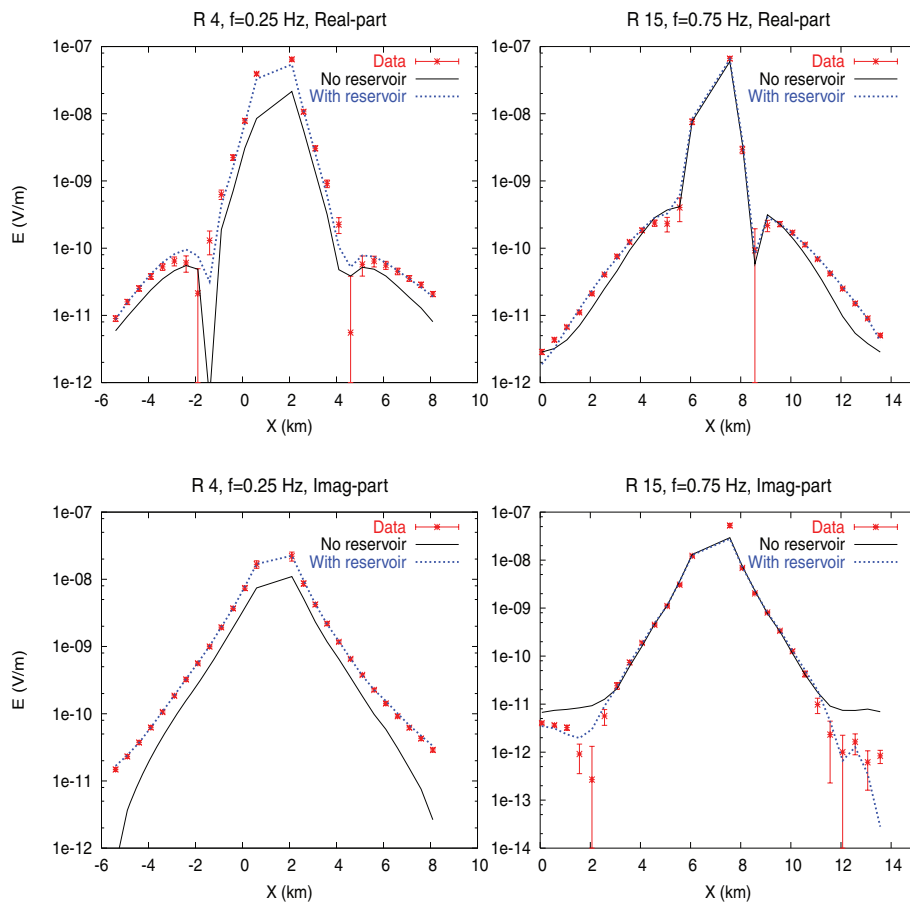


Figure 23. Data fits produced from TWGP inversion (blue curves) in comparison with a non-reservoir model (black curves), exemplified for the source positions R4 and R15 and both frequencies $f_1 = 0.25$ Hz and $f_2 = 0.75$ Hz.

achieved with the grid separation scheme show that 3-D CSEM inversion is now feasible within reasonable times, using mid-sized, parallel cluster computers.

The efficient usage of computer resources by combining two different levels of parallelization is further essential for treatment of data sets of arbitrarily large sizes.

Both the synthetic results and field data inversion examples show relatively sharp images of the known resistive targets. Here, using proper parameter constraints has proven to be extremely valuable in avoiding conductivity overshoots, which are prone to happen in unbounded inversions, particularly in the case of noisy data.

Including the source signature estimation, as shown in the synthetic studies, indicates significant potential for correcting for unwanted data distortions directly within the imaging process. Although a potentially very useful additional tool, it has to be emphasized that a careful data pre-processing still remains very important to ensure maximum data integrity.

ACKNOWLEDGMENTS

This work was carried out at Lawrence Berkeley National Laboratory, with base funding provided by the ExxonMobil Corporation and the United States Department of Energy, Office of Basic Energy Sciences, under contract DE-AC02-05CH11231. We wish to thank the German Alexander-von-Humboldt Foundation for support of MC through a Feodor-Lynen Research Fellowship. The authors also

express their gratitude to Statoil for access to the Troll field data set and the permission to publish the Troll imaging results. We also acknowledge Erika Gasperikova of LBNL for additional processing of the Troll field data, and Dmitriy A. Pavlov of ExxonMobil for many fruitful discussions.

REFERENCES

- Alumbaugh, D.L., Newman, G.A., Prevost, L. & Shadid, J.N., 1996. Three-dimensional wideband electromagnetic modeling on massively parallel computers, *Radio Sci.*, **31**, 1–24.
- Carazzone, J.J., Burtz, K.E., Green, K.E. & Pavlov, D.A., 2005. Three-dimensional imaging of marine CSEM data, *SEG Techn. Prog. Exp. Abstr.* **24**, 575–578.
- Commer, M. & Newman, G.A., 2005. An accelerated time domain finite difference simulation scheme for three-dimensional transient electromagnetic modeling using geometric multigrid concepts, *Radio Sci.*, **41**, RS3007, doi:10.1029/2005RS003413.
- Commer, M., Helwig, S.L., Hördt, A., Scholl, C. & Tezkan, B., 2006. New results on the resistivity structure of Merapi Volcano (Indonesia), derived from three-dimensional restricted inversion of long-offset transient electromagnetic data, *Geophys. J. Int.*, **167**, 1172–1187.
- Eidesmo, T., Ellingsrud, S., MacGregor, L.M., Constable, S., Sinha, M.C., Johansen, S., Kong, F.N. & Westerdahl, H., 2002. Sea Bed Logging (SBL), a new method for remote and direct identification of hydrocarbon filled layers in deepwater areas, *First Break*, **20**, 144–152.
- Ellingsrud, S., Sinha, M.C., Constable, S., MacGregor, L.M., Eidesmo, T. & Johansen, S., 2002. Remote sensing of hydrocarbon layers by seabed

- logging (SBL): results from a cruise offshore Angola, *Leading Edge*, **21**, 972–982.
- Gray, D.I., 1987. Troll, in *Geology of the Norwegian Oil and Gas Fields*, pp. 389–401, ed. Spencer, A.M., Graham and Trotman, London.
- Haber, E. & Oldenburg, D., Joint inversion: a structural approach, *Inverse Problems*, **13**, 63–77.
- Hoversten, G.M., Constable, S.C. & Morrison, H.F., 2000. Marine magnetotellurics for base-of-salt mapping: Gulf of Mexico field test at the Gemini structure, *Geophysics*, **65**, 1476–1488.
- Hoversten, G.M., Røsten, T., Hokstad, K., Alumbaugh, D.L., Horne, S. & Newman, G.A., 2006. Integration of multiple electromagnetic imaging and inversion techniques for prospect evaluation, *SEG Techn. Prg. Exp. Abstr.*, **25**, 719–723.
- Hoversten, G.M., Newman, G.A., Geier, N. & Flanagan, G., 2006. 3D modeling of a deepwater EM exploration survey, *Geophysics*, **71**, G239–G248.
- Hu, J.J., Newman, G.A. & Tuminaro, R.S., 2003. An Algebraic multigrid method for Maxwell's equations in the frequency domain, *Progress in Electromagnetics Research Symposium (PIERS)*, 13–16 October 2003, Honolulu, Hawaii, page 222.
- Johansen, S.E., Amundsen, H.E. F., Røsten, T., Ellingsrud, S. & Eidesmo, T., 2005. Subsurface hydrocarbons detected by electromagnetic sounding, *First Break*, **23**, 31–36.
- MacGregor, L. & Sinha, M., 2000. Use of marine controlled-source electromagnetic sounding for sub-basalt exploration, *Geophys. Prospect.*, **48**, 1091–1106.
- Moskow, S., Druskin, V., Habashy, T., Lee, P. & Davydchewa, S., 1999. A finite difference scheme for elliptic equations with rough coefficients using a cartesian grid nonconforming to interfaces, *SIAM J. Numer. Anal.*, **36**, 442–464.
- Newman, G.A. & Alumbaugh, D.L., 1997. Three-dimensional massively parallel electromagnetic inversion—I. Theory, *Geophys. J. Int.*, **128**, 345–354.
- Newman, G.A. & Alumbaugh, D.L., 2000. Three-dimensional magnetotelluric inversion using non-linear conjugate gradients, *Geophys. J. Int.*, **140**, 410–424.
- Newman, G.A. & Alumbaugh, D.L., 2002. Three-dimensional induction logging problems, Part 2: a finite-difference solution, *Geophysics*, **67**, 484–491.
- Newman, G.A. & Hoversten, G.M., 2000. Solution strategies for two- and three-dimensional electromagnetic inverse problems, *Inverse Problems*, **16**, 1357–1375.
- Newman, G.A. & Boggs, P.T., 2004. Solution accelerators for large-scale three-dimensional electromagnetic inverse problems, *Inverse Problems*, **20**, 151–170.
- Nocedal, J., 1995. Conjugate gradient methods and nonlinear optimization, in *Proc. Conf. Linear and Nonlinear Conjugate Gradient-Related Methods*, pp. 9–23, eds Adams, L. & Nazareth, J.L., SIAM, Philadelphia.
- Pratt, R.G., 1999. Seismic waveform inversion in the frequency domain, Part 1: theory and verification in a physical scale model, *Geophysics*, **64**, 888–901.
- Schlumberger, 1987. *Log Interpretation Principles*, Schlumberger Educational Services, Houston, Texas.
- Weiss, C.J. & Constable, S., 2006. Mapping thin resistors and hydrocarbons with marine EM methods, Part II—modeling and analysis in 3D *Geophysics*, **71**, G321–G332.
- Yee, K.S., 1966. Numerical solution of initial boundary value problems involving Maxwell's equations in isotropic media, *IEEE Trans. Ant. Prop.*, AP-14, 302–307.